

RIEMANNIAN-MANIFOLD STEERING: GEOMETRY-AWARE GENERATIVE AUTOENCODERS FOR LABEL-FREE STEERING

Narmeen Oozeer
Martian

Shivam Raval
Harvard University

Philip Quirke
Martian

Manikandan Ravikiran
Thoughtworks

Jeff Phillips
University of Utah

Shriyash Upadhyay
Martian

Amirali Abdullah
Thoughtworks

ABSTRACT

Steering a language model - intervening on its internal activations to change downstream behaviour - has recently expanded beyond linear interpolation to nonlinear methods such as angular and kernelized steering, which define intervention transformations without learning an explicit geometry over paths in activation space. Freshly introduced geometry-aware manifold methods do learn such a geometry, but require labelled class centroids together with prescribed cyclic or sequential structure. These assumptions restrict where manifold steering can be applied, since existing constructions require labelled centroids and compatible boundary conditions. We recast manifold steering more broadly as **Riemannian geodesic computation** on activation space, recovering linear and labelled-spline steering as geodesics under particular choices of metric. A principled metric within this framework is the output-space Hellinger distance pulled back to activations; we approximate this with a learned encoder trained on output distances over a small concept-token schema - no per-prompt labels, no topology prior, and no per-task curve fitting. Empirically, the method reliably drives the model onto the target class across all tasks in a standard four-task language-model arithmetic benchmark, while following more behaviourally natural trajectories than baselines on smaller output spaces. We thereby provide a unified Riemannian framework for manifold steering together with a schema-supervised, label-free instantiation that operates without labelled centroids or prescribed boundary conditions.

1 INTRODUCTION

Steering a neural network, intervening on internal activations to controllably change downstream behaviour, benefits from respecting the curved, low-dimensional structure that recent work argues language-model activations exhibit (Wurgaft et al., 2026; Vu & Nguyen, 2025; Raval et al., 2026; Engels et al., 2025; Modell et al., 2025; Park et al., 2025; Kantamneni & Tegmark, 2025; Gurnee et al., 2024; Karkada et al., 2026; Prieto et al., 2026). We do not claim a true smooth low-dimensional activation manifold exists in any model-theoretic sense: the data we operate on are a few-hundred distinct facts $\times \sim 21$ paraphrases per task, finite and clustered. The claim we work from, and that prior work supports empirically, is weaker: a useful low-dimensional *approximation* can be learned, and interventions that follow it produce smoother behavioural trajectories than interventions that ignore it. Interventions that ignore the structure altogether (a straight line in activation space) either fail to move the model or produce incoherent intermediate states; the interventions that follow it (a fitted spline) produce smooth behavioural trajectories but at a price in supervision.

Wurgaft et al. (2026) make this concrete on language-model activations: they fit a cubic spline through per-class activation centroids and steer along its arc. Their construction works, but it requires the analyst to supply (i) per-class activation centroids as spline knots and (ii) a knot ordering with a boundary-condition choice (periodic for weekdays and months, natural for letters and ages) that

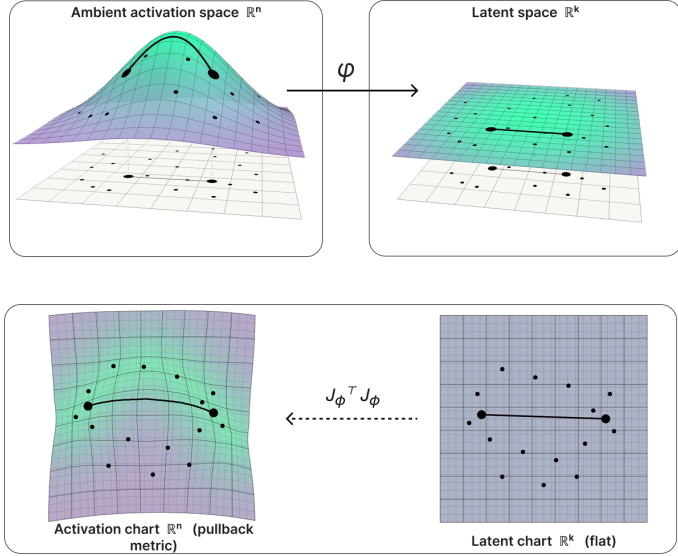


Figure 1: **Manifold steering as Riemannian geodesic computation.** A GAGA encoder φ maps the ambient activation space $\mathcal{A} = \mathbb{R}^n$, a curved activation manifold (top-left), into a latent space \mathbb{R}^k (top-right). The encoder is trained so that latent Euclidean distance reproduces a target distance d between training points: either the PHATE diffusion distance on activations (activation geometry) or the Hellinger distance d_H on output distributions (behaviour geometry). Either choice is represented within the same flat latent chart: φ learns a coordinate system on \mathbb{R}^k in which the chosen target distance becomes ordinary Euclidean distance, so geodesics are straight lines there (bottom-right). The geometry resurfaces when this flat metric is pulled back through the encoder Jacobian $J_\varphi^T J_\varphi$, warping the activation chart (bottom-left) so steering trajectories curve to follow the learned geometry.

commits to the conceptual topology before fitting. The class labels and the boundary-condition choice both do real work; relax either and the construction does not apply.

Wurgaft et al. (2026, §3.4) take a first step toward unifying steering strategies geometrically, defining three analytical metrics (G_I flat, G_E density-based, G_F output pullback) under which their linear, manifold, and pullback steering arise as geodesics. We approach the same problem from a different, more data-driven angle: rather than specifying the metric analytically, we *learn* it from data via an encoder pullback (fig. 1), which (i) makes metric and solver orthogonal design axes and (ii) opens supervision modes (schema-supervised output distances, in our case) that analytical metrics cannot use. It also reveals that the existing alternatives are not really alternatives. Linear interpolation is the geodesic under $g = I$. Wurgaft et al. (2026)’s labelled cubic spline arises in their framework as the geodesic of a density-based metric G_E whose minima coincide with the spline through the class centroids; restricted to that spline, G_E -geodesics agree with the first fundamental form $g = J_s^T J_s$ of the spline parameterisation s . Both baselines are then special cases of our framework, not competing methods.

The principled choice of g within this framework is the pullback of the output-space Hellinger metric through the rest-of-the-network forward map F (Wurgaft et al., 2026; Amari, 2016): $G_F = J_F^T g_y J_F$. This is the metric Wurgaft et al. (2026) formally specify but do not realize via explicit-Jacobian autodiff: they access G_F implicitly by directly optimizing activation paths to induce a target trajectory on \mathcal{M}_y (their §3.3, $R^2 \in [0.47, 0.78]$). Computing J_F explicitly requires per-pair passes through F and is expensive as a training signal at scale. We replace this analytical metric with a cheap learned *surrogate*: a Geometry-Aware Generative Autoencoder (GAGA; Sun et al., 2025) whose encoder φ is trained to match a target distance source, and whose induced pullback $g_\varphi = J_\varphi^T J_\varphi$ acts as a stand-in for G_F . The surrogate is not equal to G_F (different supervision sources target different

geometries, and the encoder’s geometry can diverge from F ’s along the path), but we evaluate it empirically on the same behavioural metric (E_{BC} on output distributions) that G_F would optimise. Crucially, the encoder is supervised by an output-space distance over a small fixed *concept-token schema*: it requires no per-prompt class labels and no boundary-condition prior. We refer to this as *schema-supervised, label-free*, not unsupervised, because the choice of concept tokens (e.g. the seven weekday tokens) and the evaluator that scores output Hellinger distances are fixed inputs to the training pipeline, even though no individual prompt is labelled.

Contributions.

1. **Framework.** Wurgaft et al. (2026, §3.4) cast linear, manifold, and pullback steering as geodesics under three analytically specified metrics (G_I, G_E, G_F). We reframe metric choice as a *learning* problem: rather than designing G from a density or energy prior, we learn an encoder φ whose pullback $J_\varphi^\top J_\varphi$ approximates the principled target G_F from data. This change of lens (i) separates metric from solver as orthogonal design axes (letting any metric pair with any compatible solver) and (ii) admits supervision sources unavailable to analytical metrics, including the output-Hellinger distances we use, which require no labelled centroids and no boundary-condition prior (section 3).
2. **Method.** We propose a cheap, schema-supervised *surrogate* for G_F : a GAGA encoder trained on output-Hellinger distances over a small concept-token schema, label-free at the prompt level and boundary-condition-free (section 6).
3. **Empirical Results.** On the four arithmetic tasks of Wurgaft et al. (2026) the output-grounded raw-4096 variant lands the target class decisively on every task (waypoint legibility $\geq 99\%$; endpoint target probability $1.4\text{--}5.7\times$ the better baseline), wins behaviour-fidelity E_{BC} on the two small output spaces (weekdays 7: $12\times$; months 12: $2.4\times$), and loses E_{BC} on the two larger ones (letters 22, ages 91); a 22-cell PCA(64) encoder-variant ablation shows the effect is specific to the raw-4096 output-grounded representation (section 8).

A reader new to Riemannian-geometry terminology may find section 2 useful; a reader who prefers to skip the framing and read empirics first may go directly to section 6.

2 NOTATION AND GLOSSARY

This section assembles terminology used throughout the paper, oriented toward readers from mechanistic interpretability who may be encountering manifold-learning concepts for the first time. We assume comfort with linear algebra, basic probability, and standard transformer activations. Definitions here are deliberately informal; pointers to standard textbook treatments (Lee, 2003) are given where appropriate.

Manifold (smooth, embedded). A d -dimensional smooth manifold $\mathcal{M} \subset \mathbb{R}^n$ is a subset that locally resembles \mathbb{R}^d ; every point has a neighborhood that can be smoothly mapped to and from an open subset of \mathbb{R}^d . Throughout this paper $d \ll n$: activation manifolds are typically 1- or 2-dimensional structures embedded in $n = 4096$ -dimensional residual streams.

Intrinsic vs. ambient dimension. The *ambient* dimension is the dimension of the space the manifold lives in (n); the *intrinsic* dimension is the dimension of the manifold itself (d). For days of the week, the ambient dimension is the residual-stream width; the intrinsic dimension is one (a circle).

Riemannian metric / metric tensor. A Riemannian metric g assigns to each point a positive (semi-)definite bilinear form $g(h)$ on the tangent space at h . In coordinates, $g(h)$ is an $n \times n$ symmetric positive (semi-)definite matrix. The metric defines length: $L_g(\pi) = \int_0^1 \sqrt{\dot{\pi}(t)^\top g(\pi(t)) \dot{\pi}(t)} dt$. Different metrics produce different notions of “shortest path”.

Geodesic. A geodesic between h_0 and h_1 under metric g is the path that minimizes L_g . Under the flat metric $g = I$, geodesics are straight lines; under non-flat metrics they curve to follow the manifold’s intrinsic geometry.

Pullback metric. Given a smooth map $\phi : \mathcal{A} \rightarrow \mathbb{R}^k$ (e.g. an encoder), the *pullback* of the Euclidean metric on \mathbb{R}^k through ϕ is the metric

$$g(h) = J_\phi(h)^\top J_\phi(h), \quad J_\phi(h) = \frac{\partial \phi}{\partial h}(h) \in \mathbb{R}^{k \times n}.$$

This metric measures distances in \mathcal{A} as they “feel” from ϕ ’s perspective: two points are far apart under g if their encodings are far apart in \mathbb{R}^k . Pullback metrics transport geometric structure from a chosen latent space back to the original activation space.

Encoder Jacobian and $J_\phi^\top J_\phi$. For a trained encoder, $J_\phi^\top J_\phi$ encodes how much each ambient direction stretches or compresses under ϕ . Directions *on* the activation manifold are mapped near-isometrically (eigenvalues ≈ 1); directions *off* the manifold are heavily compressed (small or zero eigenvalues). This is what gives the pullback metric its manifold-respecting character: moving on-manifold is cheap, moving off-manifold is expensive.

Isometry / scaled isometry. Two metric spaces (\mathcal{M}_1, d_1) and (\mathcal{M}_2, d_2) are *isometric* if there is a bijection ϕ with $d_2(\phi(x), \phi(y)) = d_1(x, y)$ for all x, y ; *scaled isometric* if $d_2(\phi(x), \phi(y)) = c \cdot d_1(x, y)$ for some $c > 0$.

Activation space \mathcal{A} . $\mathcal{A} = \mathbb{R}^n$, the residual stream at a chosen (layer, token-position) of the transformer. Throughout we use Llama-3.1-8B layer 28, so $n = 4096$.

Probability simplex Δ^k . $\Delta^k = \{p \in \mathbb{R}_{>0}^k : \sum_i p_i = 1\}$: k -class probability distributions with strictly positive entries. Restricting to strictly positive entries makes Δ^k a smooth manifold of dimension $k - 1$.

Behavior space \mathcal{Y} . $\mathcal{Y} = \Delta^{|\mathcal{Z}|}$, the open probability simplex over a conceptual domain \mathcal{Z} . A point in \mathcal{Y} is a distribution over concept tokens (e.g. over the seven days of the week, plus an “other” class). We embed \mathcal{Y} in Hellinger space via $p \mapsto \sqrt{p}$ to linearize.

Hellinger distance. $d_H(p, q) = \frac{1}{\sqrt{2}} \|\sqrt{p} - \sqrt{q}\|_2$. The embedding $p \mapsto \sqrt{p}$ takes Δ^k to the positive orthant of the unit sphere in \mathbb{R}^k ; under this embedding, Hellinger distance is just Euclidean distance.

Bhattacharyya distance. $d_{BC}(p, q) = -\log \sum_i \sqrt{p_i q_i} = -\log \langle \sqrt{p}, \sqrt{q} \rangle$. We use it to measure naturalness of a behavioral trajectory: low values mean the trajectory stays close to the manifold of natural model outputs.

Linear representation hypothesis (LRH). The hypothesis that high-level features are encoded as linear functions of activations (Park et al., 2023; Elhage et al., 2022). Under LRH, steering reduces to vector arithmetic. Empirical evidence is mixed: LRH holds for some features but not for others, including the cyclic and graph-structured concepts we study.

Activation centroid. The mean of activations sharing a label (e.g. all activations whose target answer is “Wednesday”). We use centroids only at evaluation time; Wurgaft et al. (2026) additionally use them at fit time, as the knots of their cubic-spline activation manifold.

PHATE diffusion-potential distance. PHATE (Potential of Heat-diffusion for Affinity-based Transition Embedding) (Moon et al., 2019) computes pairwise distances by (a) building a k NN graph over the data, (b) running a diffusion process on it for t steps, and (c) measuring a log-difference of resulting distributions. PHATE distances respect manifold geodesics: two points close in Euclidean distance but on different parts of the manifold get a large PHATE distance. GAGA’s distance-matching loss is supervised by PHATE distances.

Steering / activation steering. Modifying internal activations during a forward pass to alter behavior. The classical recipe is *linear steering*, $h \mapsto h + \alpha v$. *Manifold steering* replaces this with paths that follow the activation manifold’s curvature. *Learned manifold steering* (this work) replaces it with paths that follow a manifold recovered from the data.

Causal mediation / intervention. The methodology of replacing a chosen activation with a target value during a forward pass and observing the effect on output (Geiger et al., 2021; 2025). We use pyvene-style interventions (Wu et al., 2024) as a black box.

Naturalness energy E_{BC} . For a behavioral trajectory $\gamma : [0, 1] \rightarrow \mathcal{Y}$ induced by a steering path, $E_{BC}(\gamma) = \int_0^1 d_{BC}(\gamma(t), \mathcal{M}_y) \mathcal{M} dt$ (Wurgaft et al., 2026). Low E_{BC} means the trajectory stays in the region of plausible model outputs.

$\mathcal{M}_h, \mathcal{M}_y$. $\mathcal{M}_h \subset \mathcal{A}$ is the activation manifold (this paper: the image of GAGA’s decoder). $\mathcal{M}_y \subset \mathcal{Y}$ is the behavior manifold (a cubic spline through Hellinger-embedded behavior centroids; we keep this identical to Wurgaft et al. (2026), see section 7).

3 MANIFOLD STEERING AS RIEMANNIAN GEODESIC COMPUTATION

Given a Riemannian metric g on activation space $\mathcal{A} = \mathbb{R}^n$, steering between two endpoints h_0, h_1 is the geodesic of g joining them. This is the framing this paper adopts. Under it, the design space for a steering method has two orthogonal axes: *which metric* we put on \mathcal{A} , and *how we compute geodesics* under that metric. The first is a modeling choice about the geometry that the LM induces on its own activations; the second is a numerical-methods choice. Wurgaft et al. (2026, §3.4) name three analytical metrics (G_I, G_E, G_F) and tie each to a single solver (closed-form for linear and spline, path-level L-BFGS for pullback). We instead treat the metric itself as something to be learned from data, and metric and solver as orthogonal design choices. The learned-metric lens locates linear and labelled-spline steering as analytical-metric special cases, identifies G_F as the principled analytical target, and admits a new class of methods (learned-Jacobian surrogates) that the analytical-only framing does not.

The paper proceeds in three steps. In the remainder of this section we motivate the framing itself: why a Riemannian formulation in particular (section 3.1), and why the pullback construction is the principled source of a metric within it (section 3.2). Section 4 taxonomizes the four metrics this framework instantiates on language-model activations and shows that the linear and labeled-spline baselines are degenerate cases of the same construction. Section 5 taxonomizes the solvers we use under each metric.

3.1 WHY RIEMANNIAN GEOMETRY?

Linear interpolation is the Riemannian case $g = I$. The straight-line path $\pi_{\text{lin}}(t) = (1-t)h_0 + th_1$ is the geodesic of the Euclidean metric $g = I$ on \mathbb{R}^n . The “no-geometry” baseline that underwrites most prior steering work is therefore not outside the Riemannian framework: it is the flattest point.

Parametric-curve steering is Riemannian under the induced metric. For any smooth injective parameterization $s : \mathbb{R}^k \rightarrow \mathcal{A}$ with image $\mathcal{M} = s(\mathbb{R}^k)$, the differential $J_s = \partial s / \partial u$ induces a Riemannian metric on \mathcal{M} via the first fundamental form $g_{\mathcal{M}} = J_s^T J_s$ (do Carmo, 1992; Lee, 2018). The geodesics of $g_{\mathcal{M}}$, traced in the intrinsic coordinate u , are exactly the curve family of s itself. Wurgaft et al. (2026)’s labeled cubic spline is the case where s is a periodic or natural cubic spline fit through labeled class centroids and \mathcal{M} is the resulting 1-D submanifold of \mathcal{A} . Their construction is therefore not an alternative to a Riemannian framework: it is a particular Riemannian metric, namely the one induced by a hand-specified parameterization.

Riemannian geometry is the maximal smooth, local, length-based framework. Any steering method that produces smooth paths by minimizing a local cost functional is expressible as geodesic flow under some metric (Jost, 2017). Methods that fall outside this framework do so by relaxing smoothness (e.g. discrete optimal transport), determinism (diffusion-based steering), or locality (global path-optimization with non-local constraints). We adopt the Riemannian framing because: (i) it subsumes the existing baselines as special cases, (ii) it cleanly separates “which geometry” from

“how we compute paths under it,” and (iii) it gives access to the mature machinery of Riemannian solvers (Arvanitidis et al., 2018; Sun et al., 2025).¹

3.2 WHY A PULLBACK METRIC?

The framework above leaves open which metric we put on \mathcal{A} . There is no canonical answer, but there is a canonical *construction*: the pullback metric.

The pullback construction reduces metric design to target-space choice. For any smooth map $\phi : \mathcal{A} \rightarrow \mathcal{C}$ with a meaningful metric $g_{\mathcal{C}}$ on the codomain, the pullback $g(h) = J_{\phi}(h)^{\top} g_{\mathcal{C}} J_{\phi}(h)$ is the unique metric on \mathcal{A} making ϕ a local isometry *into* \mathcal{C} (Lee, 2003, Ch. 13). We emphasise that the isometry is to the codomain only (a definitional property), not to whatever “true” behaviour geometry the model induces in practice.

Rank deficiency and the ϵI regulariser. When ϕ maps to a codomain of dimension $k \ll \dim \mathcal{A}$, the pullback $J_{\phi}^{\top} J_{\phi}$ has rank at most k and is therefore rank-deficient PSD, not a Riemannian metric on the full ambient space. In every operational use of G_{ϕ} in this paper (sections 4 and 5), we replace it by the regularised form $G_{\phi} + \epsilon I$ with $\epsilon > 0$ small. This makes the metric a bona-fide, strongly anisotropic Riemannian metric: the k directions captured by J_{ϕ} retain their target-pullback weights, while the remaining $\dim \mathcal{A} - k$ directions are allbut-isotropic at cost ϵ . Without the ϵI term the construction is degenerate (sub-Riemannian); the regulariser is not a numerical convenience but a structural part of the metric we actually use. *Both the analytical G_F formally specified by Wurgaft et al. (2026, Def. 1 eq. 7) and the learned encoder pullback we propose (section 6) inherit this regularisation.*

Why pull back from outputs. Choosing a metric on activations reduces to choosing a target space \mathcal{C} whose geometry we already trust, plus the differentiable map ϕ . This is a familiar move in information geometry, where the Fisher metric is itself a pullback of L^2 through a parametric family of distributions (Amari, 2016), and in deep generative modeling, where decoder Jacobians pull back from a latent space (Arvanitidis et al., 2018; Shao et al., 2018; Kalatzis et al., 2020; Chadebec et al., 2022).

Output behavior space is the natural target for activation steering. Activations matter only insofar as they shape outputs: two activations that decode to the same output distribution are behaviorally equivalent regardless of their Euclidean distance. A metric on activation space should therefore identify behaviorally-equivalent activations as having distance zero and separate behaviorally-distinct ones. The Euclidean metric $g = I$ fails this: it weights all 4096 residual-stream directions equally despite most being behaviorally inert. The pullback from output behavior space succeeds by construction: the metric is zero in directions where the output is unchanged. Wurgaft et al. (2026)’s Definition 1 names three metrics: G_I (flat), G_E (density), and G_F (output pullback). The third, $G_F = J_{Fg_y}^{\top} J_F + \epsilon I$, is the principled target for activation-space steering and is the metric our learned surrogate approximates. With $\phi = F$ the rest-of-the-network map from activations to output distributions (in Hellinger coordinates, so that $g_{\mathcal{C}} = I$), this is exactly $G_F = J_F^{\top} J_F + \epsilon I$, the metric Wurgaft et al. (2026, Def. 1 eq. 7) formally specify and access implicitly via path-level L-BFGS but do not realize via explicit Jacobians. The framework’s principled metric has a 25-year information-geometric pedigree.

The remaining design choice is how to instantiate the principled output-pullback in practice. We examine three instantiations in section 4: the flat case ($g = I$), the implicit case (the spline-induced first fundamental form), and a learned-encoder *surrogate* (GAGA’s $J_{\phi}^{\top} J_{\phi} + \epsilon I$). The first two correspond to existing baselines; the third is the schema-supervised, label-free instantiation we propose. We treat the analytical G_F (computed via autodiff through the rest-of-network forward map) as the *target* the surrogate is trying to match, not as a fourth method on the empirical table; it is not implemented in this work, and a tractable design that exploits the layer-28 injection point (only a

¹A careful reader will note that “smooth local length-based” is more precise than “any smooth path-finding method.” The strict generalization beyond Riemannian to Finsler geometry permits anisotropic but homogeneous length functionals; for the length functionals we use, $\int \sqrt{\pi^{\top} g \pi} M dt$ with symmetric positive-definite g , the Riemannian case is sufficient.

~ 3 -layer tail of the network is downstream, allowing JVP-based extraction instead of a full Jacobian) plus several open design choices (prompt-dependence, solver unification) are left as follow-up work.

4 CHOICES OF METRIC ON ACTIVATION SPACE

The Riemannian framing of section 3 reduces “how should we steer” to “which metric on \mathcal{A} do we put.” Within this framing, the labelled cubic spline of Wurgaft et al. (2026) is a degenerate special case: it is the geodesic of the first fundamental form induced by a hand-specified parameterisation s , restricted to the spline’s image and solved in closed form. Relaxing any of (a) the parameterisation choice, (b) the metric’s coupling to that parameterisation, or (c) the closed-form solver yields a more general method. Table 6 enumerates the three instantiations we report in this paper, ordered left-to-right by conceptual distance from the principled output-pullback target identified in section 3.2. The encoder-pullback column is further decomposed in section 6.1 into two supervision modes (unsupervised activation-distance and schema-supervised output-distance). Per section 3.2, every metric below that has rank less than $\dim \mathcal{A}$ is used in its regularised form $G + \epsilon I$ with $\epsilon > 0$ small; we suppress the regulariser in the table for readability.

4.1 FLAT METRIC: $g = I$

The Euclidean metric weights all 4096 directions of the residual stream equally. Its geodesic between two activations is the straight line. As discussed in section 3.2, this metric fails to identify behaviorally-equivalent activations: two activations that decode to the same output distribution receive nonzero distance whenever they differ in any direction. We include it as a baseline.

4.2 LABELED SPLINE: IMPLICIT METRIC FROM A HAND-SPECIFIED PARAMETERIZATION

Given a chosen ordering of class centroids $\{\bar{h}_z\}_{z \in \mathcal{Z}}$ (cyclic for weekdays and months, sequential for letters and ages) and boundary conditions matching the topology, a cubic spline $s : [0, |\mathcal{Z}|] \rightarrow \mathcal{A}$ is fit by minimizing curvature subject to passing through every centroid. The induced first fundamental form on s ’s image $\mathcal{M}_s = s(\mathbb{R})$ is $g_{\mathcal{M}_s} = J_s^\top J_s$ (do Carmo, 1992; Lee, 2018), and the geodesic between two centroid endpoints $\bar{h}_{z_0}, \bar{h}_{z_1}$ is the spline arc connecting them, evaluated in closed form. The construction has two limitations: it requires class labels and a boundary-condition prior at fit time, and it does not generalize beyond centroid pairs: π_{spline} is undefined for endpoints not on \mathcal{M}_s .

4.3 THE PRINCIPLED TARGET: ANALYTICAL J_F PULLBACK

The metric Wurgaft et al. (2026, Def. 1 eq. 7) formally specifies is

$$G_F(h) = J_F(h)^\top g_y J_F(h) + \epsilon I, \quad J_F(h) = \frac{\partial F}{\partial h}(h), \quad (1)$$

where $F : \mathcal{A} \rightarrow \mathcal{Y}$ is the rest-of-the-network map from the chosen layer’s activations to the output distribution restricted to $\mathcal{Z} \cup \{\text{other}\}$, and g_y is the behavior-space metric. Working in Hellinger coordinates (\sqrt{p} outputs) sets $g_y = I$ and reduces G_F to $J_F^\top J_F + \epsilon I$. The ϵ regulariser absorbs the rank deficiency $\text{rank}(J_F) \leq |\mathcal{Z}| + 1 \ll \dim \mathcal{A}$ (see the general ϵI treatment in section 3.2). This is the principled target within the pullback framework. Wurgaft et al. (2026) access it implicitly via direct L-BFGS optimization of activation paths (their §3.3); we instead realize it explicitly, via reverse-mode autodiff through the LM at every waypoint. Exploiting the layer-28 injection point makes this tractable, since only the ~ 3 -layer tail downstream is needed. We compute it directly on weekdays as a method-validity check - the learned surrogate reproduces it (section 8.1) - and otherwise use the cheaper learned encoder pullback (section 4.4) as the surrogate throughout.

4.4 LEARNED ENCODER PULLBACK (GAGA): THE SURROGATE WE USE

A GAGA encoder $\varphi : \mathcal{A} \rightarrow \mathbb{R}^k$ trained on pairwise distances $\{\mathbf{d}_{ij}\}$ from a corpus of activations induces a learned pullback metric $G_\varphi(h) = J_\varphi(h)^\top J_\varphi(h) + \epsilon I$. Crucially, $\{\mathbf{d}_{ij}\}$ ranges over the full corpus of training activations, not the class centroids alone: every datapoint constrains the learned geometry, so the GAGA manifold is fit to the entire activation cloud and its pullback metric is defined

at every point of \mathcal{A} . This is unlike the labelled spline (section 4.2), whose manifold is pinned only at the $|\mathcal{Z}|$ class centroids and whose geodesic is undefined away from that curve. The ϵI term is structural (see section 3.2): without it, G_φ has rank at most k and is sub-Riemannian on the ambient $\dim \mathcal{A}$ -dimensional space. The choice of distance source $\{\mathbf{d}_{ij}\}$ shapes which target geometry the surrogate follows. We instantiate two supervision modes, GAGA-PHATE (unsupervised, activation-distance) and GAGA-Out (schema-supervised, output-distance), with full architecture, losses, and the raw-4096 vs. PCA(64) ambient-asymmetry disclosure deferred to sections 6.1 and 6.5. The empirically winning variant in this paper is GAGA-Out; GAGA-PHATE appears as one of the inert PCA(64) variants in the encoder ablation (sections G and 8.5).

5 SOLVERS: HOW WE COMPUTE GEODESICS UNDER A CHOSEN METRIC

Given a metric from section 4, we use one of three solvers to produce the geodesic between an endpoint pair. The solvers are orthogonal to the metric: any metric can be paired with any compatible solver, and running the same metric under two different solvers is itself an experiment (does the cheaper solver converge to the same geodesic as the more expensive one?). Table 7 enumerates the (metric, solver) cells we evaluate.

Closed-form. For the flat metric $g = I$ the geodesic is the straight chord; for the labeled-spline metric the geodesic is the spline arc connecting the endpoints in the spline’s intrinsic coordinate. Both are evaluated by direct evaluation, no optimization needed. These are the existing baselines.

Free-waypoint L-BFGS with the freeze-metric approximation. Discretize the path as $K = 50$ free waypoints π_0, \dots, π_K with endpoints $\pi_0 = h_0$, $\pi_K = h_1$ fixed, and minimize the discrete length functional

$$L(\pi) = \sum_{k=0}^{K-1} \sqrt{\|J(\pi_k) \Delta_k\|_2^2 + \epsilon \|\Delta_k\|_2^2}, \quad \Delta_k = \pi_{k+1} - \pi_k, \quad (2)$$

by L-BFGS on the $K - 1$ interior waypoints. The right-hand factored form avoids materializing the full $G = J^\top J$ at each waypoint, keeping memory at $O(K \cdot m \cdot D)$ with $m = \text{rank}(J) \leq |\mathcal{Z}| + 1 \ll D$. We adopt the freeze-metric approximation (Arvanitidis et al., 2018): $J(\pi_k)$ is detached from the optimizer’s graph each step, so gradients flow only through Δ_k . This is the standard discrete-Riemannian-path choice and dominates the per-iteration cost via Jacobian *evaluation*, not Jacobian backprop. The solver is metric-agnostic: we use it for the GAGA encoders and for analytical G_F with the appropriate Jacobian factor (the analytical- G_F Jacobian is supplied as a drop-in `metric_fn`; see section F.2).

Amortized parametric bridge (GeodesicBridge). Sun et al. (2025)’s `GeodesicBridge` trains a single curve generator $c_\theta : \mathcal{A} \times \mathcal{A} \times [0, 1] \rightarrow \mathcal{A}$ to produce geodesics for endpoint pairs drawn from the training activation distribution. The training objective is the encoder-pullback length integrated over the curve, plus a density penalty (Sun et al., 2025). After training, the geodesic for a new endpoint pair is a single forward pass through c_{θ^*} , shifting per-pair cost from $O(\text{path optimization})$ to $O(\text{forward pass})$. This solver is only available for the GAGA metrics, where the encoder Jacobian is the metric: training a bridge against analytical G_F would require running the LM forward at every gradient step on θ and is cost-prohibitive without approximations. Implementation details are in ??, and the asymptotic per-pair cost of every (metric, solver) cell is compared in table 10. We note one current limitation of the bridge solver itself, independent of the metric it is paired with: in preliminary runs its trained curves balloon well off the straight chord rather than tracking the encoder pullback, which we trace to the length objective lacking a sufficient on-manifold constraint. Strengthening the bridge is ongoing work pursued separately; the results in this paper are computed with the L-BFGS solver and we do not report bridge geodesics here.

What we evaluate. Holding the solver fixed and varying the metric isolates the effect of the metric: which Riemannian structure best predicts natural model behavior? This is the comparison we report — the analytical G_F against its learned encoder surrogate (section 8.1), both solved with L-BFGS, which we use for every result in section 8. The factorial also admits a solver axis (L-BFGS versus the amortized bridge); we do not report it here — the bridge has a current limitation of its own (above) that we are addressing separately — so all reported geodesics are computed with L-BFGS.

6 GAGA: A LEARNED-ENCODER SURROGATE FOR THE OUTPUT-PULLBACK METRIC

We instantiate the learned-encoder pullback of section 4.4 with the Geometry-Aware Generative Autoencoder (Sun et al., 2025); fig. 1 gives the geometric picture. An encoder $\varphi : \mathcal{A} \rightarrow \mathbb{R}^k$ is trained to match a target distance source on the data corpus; its pullback $G_\varphi(h) = J_\varphi(h)^\top J_\varphi(h) + \epsilon I$ is then used as a *surrogate* for the analytical output-pullback G_F (section 3.2). The framework admits two supervision modes for φ , one unsupervised, one schema-supervised, and the empirically winning instantiation in this paper is the schema-supervised one. We describe both modes here so the framework is honest about the design space, and we are explicit about which one produces the headline numbers of section 8.

6.1 TWO SUPERVISION MODES FOR THE ENCODER

Mode 1: unsupervised activation-distance supervision (GAGA-PHATE). The encoder is trained to preserve a distance computed entirely on unlabelled activations: d_{ij}^{PHATE} , the PHATE diffusion-potential distance (Moon et al., 2019), on the per-task training-prompt cloud. PHATE constructs a graph on activations, computes diffusion potentials through it, and yields a distance metric that respects local activation-density structure. In this mode, the encoder operates on the PCA(64)-reduced activation representation used by Wurgaft et al. (2026), with latent dimension $k = 2$ (one above the intrinsic $d = 1$ so periodic structure embeds without antipodal collapse). No class labels and no output-space information are used at training time: the supervision is purely activation-geometric.

Mode 2: schema-supervised output-distance supervision (GAGA-Out). The encoder is trained on a distance computed from *output distributions*: $d_{ij}^H = \frac{1}{\sqrt{2}} \|\sqrt{p_i} - \sqrt{p_j}\|_2$, the Hellinger distance between the model’s next-token distributions p_i, p_j restricted to the concept-token schema (e.g. the seven weekday tokens for the weekdays task) plus an “other” bin. In this mode, the encoder operates on the *raw-4096* layer-28 residual stream (the ambient activation space, not a PCA-reduced subspace), with `skip_pca` training and latent dimension $k = K$ equal to the per-task class count. We call this the *GAGA-Out* variant. The supervision is schema-supervised, label-free at the prompt level, and boundary-condition-free; the concept-token schema and the Hellinger evaluator on outputs are fixed inputs to the training pipeline, but no individual prompt carries a class label.

These two modes correspond to the two empirically clean ways to ground the surrogate within the framework: the unsupervised mode trains the surrogate to follow the activation-density geometry that the model actually inhabits, while the schema-supervised mode trains it to follow the behaviour geometry that downstream outputs reveal. A priori either could win; empirically GAGA-Out wins decisively on every steering-strength metric we measure (section 8.3) and on the E_{BC} naturalness metric on the two small output spaces (table 2), while GAGA-PHATE is inert (section 8.5).

6.2 ARCHITECTURE AND LOSSES (GAGA-PHATE)

The GAGA-PHATE encoder/decoder pair $\varphi : \mathcal{A} \rightarrow \mathbb{R}^k$ and $\psi : \mathbb{R}^k \rightarrow \mathcal{A}$ are paired MLPs with widths [512, 256, 128] to k and the symmetric reverse for the decoder; each hidden layer has BatchNorm and ReLU. Training is on the PCA(64) activations, $k = 2$. Three losses are minimised jointly:

$$\mathcal{L}_{\text{dist}} = \mathbb{E}_{i \neq j} \left[(\|\varphi(h_i) - \varphi(h_j)\|_2 - d_{ij}^{\text{PHATE}})^2 \cdot e^{-\alpha d_{ij}^{\text{PHATE}}} \right], \quad (3)$$

$$\mathcal{L}_{\text{recon}} = \mathbb{E}_i [\|\psi(\varphi(h_i)) - h_i\|_2^2], \quad (4)$$

$$\mathcal{L}_{\text{cycle}} = \mathbb{E}_i [\|\varphi(\psi(\varphi(h_i))) - \varphi(h_i)\|_2^2]. \quad (5)$$

The exponential weight $e^{-\alpha d_{ij}}$ in eq. (3) (with $\alpha = 0.1$) emphasizes local-distance preservation. The total objective is $\mathcal{L} = \lambda_d \mathcal{L}_{\text{dist}} + \lambda_r \mathcal{L}_{\text{recon}} + \lambda_c \mathcal{L}_{\text{cycle}}$ with $(\lambda_d, \lambda_r, \lambda_c) = (0.9, 0.1, 0.05)$ following Sun et al. (2025)’s Stage-A recipe.

6.3 ARCHITECTURE AND LOSSES (GAGA-OUT, HEADLINE)

The GAGA-Out encoder differs from GAGA-PHATE in four places: (i) the supervising distance is d^H on outputs rather than d^{PHATE} on activations; (ii) the ambient representation is the raw layer-28 residual stream (\mathbb{R}^{4096}), not a PCA-projected subspace (`skip_pca` training); (iii) the latent dimension is set per task to the class count $k = K$ (weekdays 7, months 12, letters 22, ages 91); (iv) training adds a pointwise sqrt-output-distance loss \mathcal{L}_{pw} alongside $\mathcal{L}_{\text{dist}}$ and $\mathcal{L}_{\text{recon}}$, and drops the cycle loss; the loss weights are $(\lambda_d, \lambda_r, \lambda_{\text{pw}}) = (50, 1, 10)$ with softmax temperature $\zeta = 0.5$. The full training recipe (per-task hyperparameters, batch composition, optimisation schedule) is in section D and the design rationale (why a schema-supervised output-distance surrogate is the right target for steering) is in section 3.2.

6.4 GEODESIC CURVE SOLVER: GEODESICBRIDGE

After encoder training, geodesics between endpoint pairs in \mathcal{A} are produced by a small parametric curve generator $c_\theta : \mathcal{A} \times \mathcal{A} \times [0, 1] \rightarrow \mathcal{A}$:

$$c_\theta(h_0, h_1, t) = (1 - t)h_0 + th_1 + \sigma_q(t) \text{MLP}_\theta(\varphi(h_0), \varphi(h_1), t), \quad (6)$$

with $\sigma_q(t) = 1 - (2t - 1)^q$ an envelope vanishing at the endpoints ($q = 4$) and MLP_θ a 4-layer MLP of width 256. Training minimises the encoder-pullback length integrated over the curve, plus a density penalty pulling the curve into well-populated regions of the training activation distribution (Sun et al., 2025); see section E. At inference, the geodesic for a new endpoint pair is a single forward pass through c_{θ^*} , the amortised solver of section 5. The headline numbers of section 8 are produced with the L-BFGS solver under the GAGA-Out encoder, not with the `GeodesicBridge`; we nonetheless examine the bridge’s learned geodesics qualitatively, since they show what geometry a learned pullback metric induces.

Even PHATE supervision yields a well-behaved geodesic. Although GAGA-PHATE is not the headline encoder, its bridge-solved geodesic still has a desirable geometric property worth noting. Figure 4 overlays three paths for a representative steering pair, projected onto the top two principal components of the activation cloud: the linear chord ignores the activation geometry, the labelled spline over-curves (it must thread every class centroid in order), and the GAGA-PHATE geodesic sits between the two: curved toward the populated region of the cloud but without the spline’s sprawling detour. Figure 7 recovers the same shape across every prompt paraphrase. So even activation-only PHATE supervision, which does not win on behaviour fidelity (section 8.5), produces a geodesic with sensible, paraphrase-stable curvature. We do not dig deeper into the relative strengths of each architecture and supervision choice here; a fuller account is left to ongoing work.

6.5 INTERVENTION VIA SUBSPACE REPLACEMENT (AND THE AMBIENT ASYMMETRY)

Steering proceeds by sampling $K = 50$ waypoints π_k along the encoded geodesic and injecting each into the residual stream at layer 28. The injection rule depends on the ambient representation the encoder lives in.

PCA(64)-based methods (linear, labelled spline, GAGA-PHATE). For a carrier prompt’s uninter-vened activation $h_{\text{orig}} \in \mathbb{R}^{4096}$, with $P \in \mathbb{R}^{64 \times 4096}$ the PCA projection and P^+ its pseudo-inverse, the injected activation is

$$h_{\text{inj}} = h_{\text{orig}} + (\pi_k - P h_{\text{orig}}) P^+,$$

which replaces the in-PCA-subspace component of the activation while preserving the carrier’s off-subspace component. This matches `causalab`’s `FeatureInterpolateIntervention`.

Raw-4096 GAGA-Out. The GAGA-Out geodesic lives in the full \mathbb{R}^{4096} residual stream, and the injection is direct: $h_{\text{inj}} = \pi_k$ (no subspace decomposition; the full activation is replaced).

Ambient asymmetry. The two injection rules are *not* apples-to-apples comparisons. Linear and labelled-spline baselines steer only the 64-dim PCA subspace and retain the carrier’s off-subspace activation; GAGA-Out replaces the full 4096-dim residual stream. The headline target-drive advantage of GAGA-Out (table 3) is partly an architectural choice, not a path property: by design GAGA-Out

endows the whole representation with behaviour geometry, while the baselines are confined to a 64-dim shadow whose lift back to \mathbb{R}^{4096} is missing the natural off-subspace activation the source prompt would produce.

7 EXPERIMENTAL SETUP

Tasks and model. We use the four LM arithmetic tasks of Wurgaft et al. (2026): weekdays, months, letters, ages, with prompt templates and value sets from the `causalab` task configurations. Each task asks “what $[unit]$ is $k [units]$ after z ?” with z from a conceptual domain \mathcal{Z} of size 7 (cyclic), 12 (cyclic), 22 (sequential), and ~ 91 (sequential) respectively. Activations are extracted from Llama-3.1-8B-Instruct (Grattafiori et al., 2024) at layer 28 and the last-token position. The verified GAGA-Out runs behind every number in section 8 use the following per-task corpus sizes: **weekdays**: $n = 1029$ (49 distinct facts \times 21 paraphrases, 823/206 train/val split, seed 42); **months, letters, ages**: $n = 1100$ (1000/100 train/val split, seed 42). The weekdays headline therefore rests on only 49 distinct facts (heavily replicated by paraphrase), which is small; we revisit this as a limitation in section 10.

Sample-size motivation (not a guarantee). Aamari & Levrard (2019) prove that on a C^2 -smooth d -dimensional manifold of positive reach τ , with i.i.d. samples and small sub-Gaussian off-manifold noise, tangent-space estimation admits a rate $\varepsilon_T(n, d) \asymp (\log n/n)^{1/d}$. None of the Aamari & Levrard (2019) assumptions are verified for our data: our samples are not i.i.d. (a few-hundred distinct facts \times 21 near-duplicate paraphrases, heavily clustered); the reach τ is unknown (hidden constants scale like τ^{-1}); and the paraphrase spread is the kind of large structured off-manifold noise the theorem rules out. We therefore cite the rate as *motivation* primarily, the d -independence in the ambient dimension is the intuition we use to justify training a low-rank surrogate on a corpus of $\sim 10^3$ activations per task and make no formal guarantee.

GAGA configuration (GAGA-Out; the empirically winning variant). The headline numbers in section 8 are produced by the schema-supervised *GAGA-Out* encoder of section 6.3. Encoder/decoder MLPs with widths [512, 256, 128] to $k = K$ (the per-task class count: 7, 12, 22, 91), BatchNorm + ReLU; ambient = raw-4096 layer-28 residual stream (`skip_pca`, no PCA reduction at training time); loss weights $(\lambda_d, \lambda_r, \lambda_{pw}) = (50, 1, 10)$, softmax temperature $\zeta = 0.5$, no cycle loss; local-emphasis decay $\alpha = 0.1$; AdamW at lr = 10^{-3} ; up to 300 epochs with early stopping (patience 30) on validation distance loss. Full hyperparameter table in section D. The PCA(64)-based GAGA-PHATE variant used in the encoder ablation (section 8.5) follows the original Sun et al. (2025) recipe with $k = 2$ and $(\lambda_d, \lambda_r, \lambda_c) = (0.9, 0.1, 0.05)$; see section 6.2.

Geodesic solver. The headline numbers use the frozen **L-BFGS** geodesic solver of section 5 on top of the GAGA-Out encoder, not the amortised `GeodesicBridge` of Sun et al. (2025). The `GeodesicBridge` configuration (`CondCurve` with hidden dim 64, 3 layers, $n_{\text{steps}} = 50$, length weight 1.0, density weight 0.1, diffusion-graph initialisation) is documented in section 6.4 and used in the PCA(64) encoder ablation only.

Behavior manifold \mathcal{M}_y . For each task, \mathcal{M}_y is a dense cubic spline through Hellinger-embedded per-class output centroids, sampled at 500 points. The construction follows Wurgaft et al. (2026, §2) and is used identically by all methods, so per-pair E_{BC} differences are purely method-attributable.

Evaluation metrics. For each centroid pair (\bar{h}_i, \bar{h}_j) , we sample $K = 50$ waypoints along the geodesic, lift each from PCA(64) to the full 4096-D residual stream via subspace replacement (section F.4), and inject at layer 28 across 16 carrier prompts. We report:

- **Cumulative Bhattacharyya energy E_{BC}** (Wurgaft et al., 2026, §3.2): the headline naturalness score; lower means intermediate outputs look more like natural unintervened outputs.
- **Behavior-space arc length**: cumulative Hellinger arc of the induced output-distribution trajectory.
- **Visit-intermediates rate**: fraction of expected sequence-intermediate classes whose argmax was the model’s top-1 prediction at some waypoint along the trajectory.

We evaluate on $\binom{|Z|}{2}$ centroid pairs for weekdays (21 pairs); for months/letters/ages we sample 50 pairs deterministically (seed 42), sufficient under Aamari & Levrard (2019)’s bound for stable pullback-metric estimates on 1-D manifolds.

Compute. One NVIDIA A100 40 GB GPU per task; total wall-clock target under 12 hours per task. Asymptotic per-pair cost across methods is compared in table 10.

8 RESULTS

We evaluate the metrics of section 4 under the solvers of section 5, on the four tasks of section 7. Throughout this section, **GAGA-Out (L-BFGS)** denotes the output-grounded encoder of section 6 trained per-task (`seed0`, raw-4096 ambient) with the frozen L-BFGS geodesic solver. This is the *winning* encoder out of a family of variants we trained and evaluated; the PCA(64)-based GAGA variants (Vanilla-AE, GAGA-PHATE across $\lambda_{\text{dist}} \in \{0.1, \dots, 500\}$, GAGA-Hellinger across the same λ range) do not steer the model at all on the cells we ran (weekdays 15/15, months 7/15), with E_{BC} , legibility, and target probability all indistinguishable from the linear baseline (section 8.5, full matrix in section G). The raw-4096 output-grounded representation is the active ingredient; all main-paper results below report GAGA-Out (L-BFGS). Linear and labelled-spline baselines are evaluated in closed form. All differences reported here are $\times 2$ reproducible across independent re-runs from frozen checkpoints.

Headline. GAGA-Out reliably drives the model onto the target class on every task: legibly, decisively, and far more strongly than either baseline (table 3). This is a non-trivial property of the method, not an automatic consequence of constructing a path between two centroids: the linear and labelled-spline baselines are built in a PCA(64) subspace and lifted back to the residual stream, and the lifted endpoints often do not actually put the target token in the model’s top-1 (the spline reaches top-1 at the target on only 29% of weekdays pairs and 42% of letters pairs; see section 8.3). Whether the *route* taken by a method that does land the target is behaviourally natural depends on the size of the output space: on the two small tasks (weekdays, 7 classes; months, 12) GAGA wins E_{BC} by $12\times$ and $2.4\times$ over the better baseline; on the two larger tasks (letters, 22; ages, 91) GAGA still lands the target but takes a less natural path and loses E_{BC} to the baselines (table 2). We read this as the geometric promise of the method holding in full on small output spaces and partially on large ones; we return to the size-dependence in section 10.

8.1 ANALYTICAL G_F : THE LEARNED ENCODER MATCHES ITS PRINCIPLED TARGET

The method rests on one assumption: that the learned encoder is a faithful stand-in for the metric it approximates. That metric is the analytical output-pullback $G_F = \bar{J}_F^T J_F + \epsilon I$ (section 4.3), which scores an activation-space direction by how much it moves the model’s output distribution. G_F is expensive — every waypoint needs a Jacobian through the rest of the network — which is exactly why GAGA-Out substitutes a small learned encoder. Before the pipeline results we test that substitution: on weekdays we compute G_F exactly, differentiating through the ~ 3 -block transformer tail above the layer-28 injection site (section F), and run the *same* L-BFGS solver under it — only the metric changes. Each metric evaluation is now a pass through three transformer blocks and the unembedding instead of the small encoder MLP: the geodesic solver keeps the same asymptotic cost, but its per-step constant grows by roughly three orders of magnitude ($\mathcal{F}/\mathcal{E} \sim 10^3$; table 10), or ~ 3 GPU-minutes per pair against ~ 30 seconds in wall-clock. That gap is the reason a learned surrogate is worth having.

The two metrics’ geodesics agree on every row of table 1. The two paths are equally natural ($E_{\text{BC}} = 0.0085$, lower is better — an order of magnitude below the linear and spline baselines), every waypoint decodes to a clean weekday (legibility 1.000), and both drive the model onto the target equally hard (0.20 probability on the target token at the path’s end, top-1 there 76% of the time). The agreement also holds geodesic-by-geodesic: lined up pair-by-pair, the G_F and encoder waypoints differ by an average of 0.2% of the endpoint distance — the encoder does not merely *score* like the principled metric, it traces the same path.

So on weekdays the cheap encoder is a sound surrogate for the expensive analytical G_F : the steering results below can be read as a property of the output-pullback geometry, not an artefact of the

Table 1: Analytical G_F vs. the learned GAGA-Out surrogate on weekdays (all $C(7, 2) = 21$ centroid pairs), with the linear and labelled-spline baselines. Both GAGA columns use the same L-BFGS geodesic solver; only the metric differs. The principled metric and the learned encoder produce behaviourally indistinguishable geodesics.

| Metric | Analytical G_F | GAGA-Out | Linear | Labelled spline |
|-------------------------------|------------------|----------|--------|-----------------|
| $E_{BC} \downarrow$ | 0.0085 | 0.0085 | 0.1014 | 0.1011 |
| legibility (top-1) \uparrow | 1.000 | 1.000 | 0.040 | 0.047 |
| target_prob_end \uparrow | 0.202 | 0.202 | 0.049 | 0.049 |
| top-1 @ end rate \uparrow | 0.762 | 0.762 | 0.286 | 0.286 |

Table 2: Cumulative Bhattacharyya energy E_{BC} along the steered trajectory; lower means each intermediate output is closer to a natural unintervened output (see section 4). Mean over the sampled centroid pairs ($n = 21$ for weekdays, the full $C(7, 2)$; $n = 50$ for the other tasks). Paired- t statistics compare GAGA-Out (L-BFGS) against the *better* baseline per task (linear for weekdays/months/ages, spline for letters). Negative t means GAGA is more natural; positive t means the baseline is more natural.

| Method (solver) | Weekdays | Months | Letters | Ages |
|--|-----------------------|-----------------------|-----------------------|-----------------------|
| Linear (closed form) | 0.1014 | 0.1116 | 0.0261 | 0.1882 |
| Labelled spline (closed form) | 0.1011 | 0.1152 | 0.0232 | 0.2076 |
| GAGA-Out (L-BFGS) | 0.0085 | 0.0456 | 0.0352 | 0.5308 |
| <i>paired-t (GAGA vs. better baseline)</i> | -34.1 | -24.8 | +14.5 | +30.6 |
| <i>p</i> | 3.3×10^{-19} | 2.3×10^{-29} | 2.7×10^{-19} | 1.3×10^{-33} |
| <i>ratio (better baseline / GAGA)</i> | $11.9 \times$ | $2.4 \times$ | $0.66 \times$ | $0.35 \times$ |

approximation. Checking how closely the surrogate tracks G_F on larger output spaces is left to future work.

8.2 BEHAVIOURAL FIDELITY ALONG THE PATH: E_{BC}

Table 2 is the headline behavioural result and the central finding of this paper. On the two small output spaces the output-grounded geodesic finds a route along which the model’s intermediate behaviour stays close to natural unintervened behaviour throughout the steered trajectory: on weekdays the cumulative Bhattacharyya energy is more than an order of magnitude lower than either baseline (0.0085 vs. 0.101, $t = -34.1$); on months it is $2.4 \times$ lower (0.0456 vs. 0.112). On the two larger output spaces the sign flips: GAGA’s path is the least natural of the three on letters (0.035 vs. 0.023) and substantially less natural on ages (0.53 vs. 0.19). The losses are statistically sharp ($p \ll 10^{-18}$ in both directions), so they are not noise. We interpret them in tandem with tables 3 and 4 below: on large output spaces GAGA pays a naturalness cost because it is the only method that decisively moves the model toward the target, whereas the baselines mostly fail to steer and so trivially stay close to their starting distribution.

8.3 STEERING STRENGTH: DOES THE PATH ACTUALLY MOVE THE MODEL?

Landing the target is not a free property. Reaching the target class does not come for free. As noted above, the linear and labelled-spline baselines are built in a PCA(64) subspace and lifted back to the raw-4096 residual stream; the lift discards the ~ 4032 off-subspace dimensions the model would naturally produce, so a baseline path can end “at the centroid” in its 64-dim working representation yet leave the model far from the target token in behaviour space. GAGA-Out constructs its geodesic in the full ambient space and does not pay this cost. Table 3 quantifies the gap.

Table 3 is the half of the story that does not flip with task size. GAGA-Out is the only method that reliably lands the target across the suite: $\geq 99\%$ of waypoints are a clean labelled class on every task (legibility), and the endpoint places $1.4\text{--}5.7 \times$ more probability mass on the target class than either baseline. Concretely, on weekdays the spline reaches the target as top-1 only 29% of the time

Table 3: Steering-strength panel. *legibility (top-1)*: fraction of waypoints whose top-1 next-token is one of the labelled class tokens. *target_prob_end*: probability mass on the target class at the path’s endpoint. *top-1 @ end*: rate at which the endpoint’s top-1 token equals the target. Higher is better in every column. Bold = best of three.

| Method | legibility (top-1) ↑ | | | |
|--------------------------|----------------------|--------------|--------------|--------------|
| | Weekdays | Months | Letters | Ages |
| Linear | 0.040 | 0.125 | 0.790 | 0.407 |
| Labelled spline | 0.047 | 0.177 | 0.808 | 0.476 |
| GAGA-Out (L-BFGS) | 1.000 | 1.000 | 0.991 | 1.000 |
| Method | target_prob_end ↑ | | | |
| | Weekdays | Months | Letters | Ages |
| Linear | 0.049 | 0.128 | 0.060 | 0.138 |
| Labelled spline | 0.049 | 0.128 | 0.060 | 0.138 |
| GAGA-Out (L-BFGS) | 0.202 | 0.467 | 0.074 | 0.785 |
| Method | top-1 @ end rate ↑ | | | |
| | Weekdays | Months | Letters | Ages |
| Linear | 0.286 | 1.000 | 0.420 | 1.000 |
| Labelled spline | 0.286 | 1.000 | 0.420 | 1.000 |
| GAGA-Out (L-BFGS) | 0.762 | 1.000 | 0.480 | 1.000 |

Table 4: Behaviour-space arc length (left) and visit-intermediates rate, the fraction of labelled in-between classes the path traverses (right). The labelled spline visits intermediates by construction; GAGA-Out does not have access to the class sequence. Bold = best of three.

| Method | Behaviour-space arc length | | | | Visit-intermediates rate ↑ | | | |
|--------------------------|----------------------------|-------|-------|--------------------|----------------------------|--------------|--------------|--------------|
| | Wd | Mo | Le | Ag | Wd | Mo | Le | Ag |
| Linear | 0.139 | 0.311 | 0.228 | 0.543 | 0.313 | 0.514 | 0.253 | 0.144 |
| Labelled spline | 0.238 | 0.926 | 0.633 | 8.135 [†] | 0.369 | 0.816 | 0.585 | 0.954 |
| GAGA-Out (L-BFGS) | 0.312 | 0.624 | 0.252 | 1.095 | 0.631 | 0.504 | 0.282 | 0.139 |

[†]The spline’s arc on ages exceeds the unit Hellinger-simplex diameter: the cubic spline through ~ 91 ordered centroids curves so aggressively that the induced output trajectory loops well beyond any chord. We read this as the spline overshooting natural variation, not a steering-strength win.

while GAGA-Out reaches it 76% of the time; on letters GAGA edges the baselines by another ~ 6 points. On months and ages all three methods nominally hit top-1@end with rate 1.0, but the target probability mass tells the real story: GAGA puts 0.47 and 0.78 on the target class respectively, against the baselines’ 0.13 and 0.14. This is a $3.4\text{--}5.7\times$ gap, and it is largest on the largest output space, where the 64-dim PCA subspace the baselines work in retains the least of the activation the model needs to actually predict the target token. Decisive, legible target-drive is thus a structural property GAGA-Out delivers and the subspace-then-lift baselines do not, independent of the naturalness story in table 2.

8.4 PATH SHAPE: ARC LENGTH AND CLASS-SEQUENCE TRAVERSAL

Table 4 resolves the visit-intermediates story. GAGA-Out visits intermediates on weekdays (0.63, the only task where any method other than the spline wins this metric) and underperforms the spline on the larger tasks: by construction the spline is the only method that has access to the labelled class order, and on ages it visits 95% of expected intermediates while GAGA visits 14%. The arc-length comparison is the cleanest evidence that GAGA actually *steers*: on every task its arc is comparable to or longer than linear, while the spline either tracks GAGA’s length (months, letters) or blows up by an order of magnitude (ages).

Table 5: Results summary, split by output-space size. “Small” = weekdays/months (7 and 12 classes). “Large” = letters/ages (22 and 91 classes). GAGA-Out wins the decisive-target-drive property on every task; it wins the natural-route property only on small output spaces.

| Property | Small tasks (Wd, Mo) | Large tasks (Le, Ag) |
|---|----------------------|-----------------------------------|
| Lands target decisively (top-1 @ end, target_prob_end) | ✓ GAGA | ✓ GAGA |
| Every waypoint is a clean labelled class (legibility) | ✓ GAGA | ✓ GAGA |
| Naturalness of the route (E_{BC}) | ✓ GAGA (12×, 2.4×) | lost to baseline (0.66×, 0.35×) |
| Walks the labelled class sequence (visit-intermediates) | GAGA on Wd only | labelled spline (by construction) |

8.5 ENCODER-VARIANT ABLATION: PCA(64) GAGA ENCODERS ARE INERT

To check that the headline above is not specific to a single hand-picked encoder, we trained a family of GAGA encoders varying both the supervision target (PHATE diffusion distance; Hellinger output distance) and the distance-loss weight ($\lambda_{\text{dist}} \in \{0.1, 1, 10, 50, 100, 250, 500\}$), plus a plain reconstruction-only Vanilla-AE baseline. These variants all share the PCA(64) ambient representation used by the linear and spline baselines. Across the 22 cells run so far (weekdays 15/15, months 7/15; the months GAGA-Hellinger family and the letters/ages sweeps are left to future work, see section G), *no* PCA(64) variant steers the model: every cell’s E_{BC} is within 0.001 of linear’s value (weekdays ≈ 0.0996 , months ≈ 0.1117); legibility top-1 is ~ 0.05 on weekdays and ~ 0.13 on months (vs. 1.000 for GAGA-Out); target-class probability at the endpoint is identical to linear’s 0.049 on weekdays and 0.128 on months across every λ and every supervision target. The λ_{dist} sweep makes no difference: the inert behaviour is the same at $\lambda = 0.1$ and at $\lambda = 500$. The full per-encoder matrix is reported in section G. The takeaway is that the steering effect documented in tables 2 and 3 is specific to the raw-4096 output-grounded representation, not a generic property of any GAGA encoder; it is the ambient space and the output-grounding, not the PHATE/Hellinger supervision in a low-dimensional latent, that does the work.

8.6 SUMMARY

Table 5 consolidates the picture. **GAGA-Out is always the strongest “get the model decisively onto the target class, legibly” method;** it is *also* the most behaviourally natural-path method only when the output space is small. As the number of classes grows, the geometry learned by an output-grounded encoder begins to disagree with the model’s true behavioural geometry along the path, even though the endpoint stays on-target. We leave a full resolution to future work. In particular, it is not yet clear whether GAGA’s steering geometry can be learned in a *lower-dimensional* representation rather than the raw 4096-dimensional residual stream: every PCA(64) encoder variant we trained is inert (section 8.5), and isolating whether that is intrinsic or an artefact of under-training is an open question we return to in section 10.

9 RELATED WORK

Activation steering and the linear representation hypothesis. A long line of work treats steering as vector arithmetic in activation space (Bau et al., 2018; Subramani et al., 2022; Turner et al., 2024; Marks & Tegmark, 2024; Rimsky et al., 2024; Li et al., 2023), justified by the linear representation hypothesis (Park et al., 2023; Elhage et al., 2022). Empirically these methods suffer from off-target effects, fluency degradation, and distributional drift (Da Silva et al., 2025). Our framing locates these methods as the flat-metric case $g = I$ (section 3.1); the limitations are then evidence that flat geometry is the wrong metric, not that steering is broken. Recent nonlinear steering methods partially relax this assumption by introducing nonlinear coordinate systems over activation space while retaining linear interpolation in the induced parameterization: Vu & Nguyen (2025) formulate steering in angular coordinates, while Raval et al. (2026) steer within a polynomial kernel-PCA parameterization motivated by curvature analyses of activation trajectories.

Geometry of neural representations. Cyclic, sequential, and graph-structured activation manifolds are documented across architectures and modalities (Engels et al., 2025; Modell et al., 2025; Park et al., 2025; Gurnee et al., 2024; Kantamneni & Tegmark, 2025; Karkada et al., 2026; Prieto et al.,

2026). Most of this work is descriptive; Engels et al. (2025) ablate the weekday circle directly. Our framework shares Riemannian language with Wurgaft et al. (2026, §3.4 and Def. 1), who first cast linear, manifold, and pullback steering as geodesics under three analytically-specified metrics. We approach metric choice differently: rather than specifying G from a density or energy prior, we learn it from data via an encoder pullback, which separates the metric and solver axes and admits supervision sources unavailable to analytical metrics.

Manifold learning and learned Riemannian metrics. Encoder-based pullback metrics have been explored for generative modeling (Arvanitidis et al., 2018; Kalatzis et al., 2020; Chadebec et al., 2022; Shao et al., 2018) and for general metric learning (Hauberg et al., 2012); PHATE (Moon et al., 2019), UMAP (McInnes et al., 2018), t -SNE (Van der Maaten & Hinton, 2008), Isomap (Tenenbaum et al., 2000), and diffusion maps (Coifman & Lafon, 2006) supply the target distances. GAGA (Sun et al., 2025) combines a PHATE distance target with a decoder, which is what licenses our intervention pipeline. Information geometry (Amari, 2016) grounds the pullback construction itself: the Fisher information metric is a pullback of L^2 through a parametric family, and our $J_F^\top J_F$ metric is its activation-space analogue.

Causal abstraction and intervention machinery. The intervention machinery underlying the \mathcal{M}_y -side evaluation comes from the causal-abstraction tradition (Geiger et al., 2021; 2025; Huang et al., 2024; Wu et al., 2024) and is shared with Wurgaft et al. (2026). We treat it as a black-box: any improvements we report apply to any activation-manifold construction that plugs into this pipeline.

Sample complexity for manifold estimation. We take intuition from Aamari & Levrard (2019)’s C^2 tangent-estimation rate; related rates for manifold recovery are due to Genovese et al. (2012) (Hausdorff) and Fefferman et al. (2016) (manifold-hypothesis testing). The intuition we use is that the rate $n \asymp \varepsilon^{-d} \log(1/\varepsilon)$ for pullback-metric estimation depends on intrinsic d rather than ambient D , which suggests that corpora of $n \sim 10^3$ activations may be sufficient to fit a low-rank surrogate on 1-D conceptual tasks even though the activation ambient is \mathbb{R}^{4096} . We do not invoke this as a guarantee: the Aamari & Levrard (2019) assumptions (i.i.d. sampling, small sub-Gaussian off-manifold noise, known positive reach) are unverified and likely violated for LLM activations: our data are not i.i.d. (paraphrase-clustered) and the reach is unknown. We cite the rate as motivation, not as a formal license, and we report sample sizes directly in section 7.

10 DISCUSSION

What the framework buys. Framing manifold steering as Riemannian geodesic computation turns steering into a problem of learning geometry over activation trajectories rather than hand-specifying them. GAGA operationalizes this viewpoint by learning a behaviour-grounded pullback geometry directly from pairwise distances, without requiring labelled class centroids, prescribed topology, or per-task curve fitting. This permits manifold steering in settings where explicit class structure is unavailable or ambiguous, while retaining a principled geometric interpretation of steering trajectories as geodesics under the learned metric. Second, it makes new combinations easy to propose: any metric in table 6 can be paired with any compatible solver in table 7, and future work introducing a new metric (e.g. LRH-derived (Park et al., 2023; Elhage et al., 2022), causal-mediation-derived, or RLHF-delta-derived) inherits all of the geodesic machinery for free. GAGA is one instantiation of the framework; the framework is the contribution.

The task-size puzzle. The puzzle in our verified data is not the supervision target but a sharp *output-space-size* split: the GAGA-Out encoder wins behaviour-fidelity E_{BC} on the two small tasks (weekdays, months) and loses it on the two larger ones (letters, ages). Steering strength (legibility, target probability at the endpoint) is decisively in GAGA-Out’s favour on every task. We read this as the schema-supervised encoder learning a useful behaviour geometry in the small-output-space regime, where the concept-token Hellinger schema is a tight description of the behaviour the model produces, but disagreeing with the model’s true behaviour geometry along the path as the output space grows: the encoder still gets the endpoint right but takes a less natural route there. Whether this is intrinsic to the framework or a consequence of under-trained encoders (single `seed0`, no training-diagnostic ablation, single supervision recipe) is an open confound, and the multi-seed and raw-4096 linear/spline control flagged in section 8.6 are the most direct follow-ups. The analytical

G_F pullback (section 4.3) is the principled target the surrogate stands in for; we compute it directly on weekdays (section 8.1) and find the learned encoder reproduces it — the analytical- G_F and GAGA-Out geodesics are behaviourally indistinguishable there. Quantifying how faithfully the surrogate tracks the target as $|\mathcal{Z}|$ grows, where GAGA-Out’s E_{BC} advantage erodes, is the natural next step.

Limitations. Four. (i) The four tasks are 1-D in the conceptual domain. Whether GAGA recovers a useful metric on multi-dimensional concept manifolds (e.g. tori, graphs) is the natural next experiment; preliminary results on the Park et al. (2025) grid task indicate the same machinery extends, but we have not measured it here. (ii) Corpus sizes are small: $n \approx 10^3$ per task with heavy paraphrase replication (weekdays rests on 49 distinct facts \times 21 paraphrases). The intuition we take from Aamari & Levrard (2019) (section 7) is that the intrinsic-dim-only rate is favourable for $d = 1$ tasks even at this size, but the rate’s assumptions (i.i.d., known reach) do not hold for our data, so we report it as motivation not as a sample-size guarantee. Higher-dimensional concept manifolds will need either larger corpora or a different distance source. (iii) We use the canonical `GeodesicBridge` of Sun et al. (2025) without its optional discriminator; the discriminator was designed for generative sampling, not interpretable interpolation, and we did not find it to help in pilot experiments. Future work where the geodesic must traverse genuinely off-data regions might benefit from the discriminator. (iv) Our supervision is schema-supervised rather than fully unsupervised: the concept-token vocabulary and the output-Hellinger evaluator are fixed inputs. A fully unsupervised variant would supervise on the full vocabulary distribution; we expect the schema restriction to be effectively a per-task projection discarding mostly-unused tokens, but have not verified this empirically.

Looking ahead. The clearest gap the framework opens is in concepts where the topology is not known in advance: partially-cyclic schedules, hierarchical ontologies, or domain-shifted graph structures. Fitting the labelled spline requires committing to a knot ordering and matching boundary conditions a priori, both awkward to elicit for partially-cyclic or hierarchical schemas; GAGA’s metric is recovered from data and the topology falls out of the latent geometry. We expect this is where the label-free framing becomes a practical, not just an aesthetic, advantage.

REFERENCES

- Eddie Aamari and Clément Levrard. Nonasymptotic rates for manifold, tangent space and curvature estimation. *The Annals of Statistics*, 47(1):177–204, 2019.
- Shun-ichi Amari. *Information Geometry and Its Applications*, volume 194 of *Applied Mathematical Sciences*. Springer, 2016.
- Georgios Arvanitidis, Lars Kai Hansen, and Søren Hauberg. Latent space oddity: on the curvature of deep generative models. In *International Conference on Learning Representations (ICLR)*, 2018.
- David Bau, Jun-Yan Zhu, Hendrik Strobelt, Bolei Zhou, Joshua B Tenenbaum, William T Freeman, and Antonio Torralba. Gan dissection: Visualizing and understanding generative adversarial networks. *arXiv preprint arXiv:1811.10597*, 2018.
- Clément Chadebec, Elina Thibeau-Sutre, Ninon Burgos, and Stéphanie Allasonnière. Data augmentation in high dimensional low sample size setting using a geometry-based variational autoencoder. *IEEE Transactions on Pattern Analysis and Machine Intelligence*, 45(3):2879–2896, 2022.
- Ronald R Coifman and Stéphane Lafon. Diffusion maps. *Applied and computational harmonic analysis*, 21(1):5–30, 2006.
- Patrick Queiroz Da Silva, Hari Sethuraman, Dheeraj Rajagopal, Hannaneh Hajishirzi, and Sachin Kumar. Steering off course: Reliability challenges in steering language models. In *Proceedings of the 63rd Annual Meeting of the Association for Computational Linguistics (Volume 1: Long Papers)*, pp. 19856–19882, 2025.
- Manfredo P. do Carmo. *Riemannian Geometry*. Mathematics: Theory & Applications. Birkhäuser, Boston, 1992. ISBN 9780817634902.

- Nelson Elhage, Tristan Hume, Catherine Olsson, Nicholas Schiefer, Tom Henighan, Shauna Kravec, Zac Hatfield-Dodds, Robert Lasenby, Dawn Drain, Carol Chen, Roger Grosse, Sam McCandlish, Jared Kaplan, Dario Amodei, Martin Wattenberg, and Christopher Olah. Toy models of superposition, 2022. URL <https://arxiv.org/abs/2209.10652>.
- Joshua Engels, Eric J. Michaud, Isaac Liao, Wes Gurnee, and Max Tegmark. Not all language model features are one-dimensionally linear, 2025. URL <https://arxiv.org/abs/2405.14860>.
- Charles Fefferman, Sanjoy Mitter, and Hariharan Narayanan. Testing the manifold hypothesis. *Journal of the American Mathematical Society*, 29(4):983–1049, 2016.
- Atticus Geiger, Hanson Lu, Thomas Icard, and Christopher Potts. Causal abstractions of neural networks. *Advances in neural information processing systems*, 34:9574–9586, 2021.
- Atticus Geiger, Duligur Ibeling, Amir Zur, Maheep Chaudhary, Sonakshi Chauhan, Jing Huang, Aryaman Arora, Zhengxuan Wu, Noah Goodman, Christopher Potts, et al. Causal abstraction: A theoretical foundation for mechanistic interpretability. *Journal of Machine Learning Research*, 26(83):1–64, 2025.
- Christopher R Genovese, Marco Perone-Pacifico, Isabella Verdinelli, and Larry Wasserman. Manifold estimation and singular deconvolution under hausdorff loss. *The Annals of Statistics*, pp. 941–963, 2012.
- Aaron Grattafiori, Abhimanyu Dubey, Abhinav Jauhri, Abhinav Pandey, Abhishek Kadian, Ahmad Al-Dahle, et al. The llama 3 herd of models, 2024. URL <https://arxiv.org/abs/2407.21783>.
- Wes Gurnee, Theo Horsley, Zifan Carl Guo, Tara Rezaei Kheirkhah, Qinyi Sun, Will Hathaway, Neel Nanda, and Dimitris Bertsimas. Universal neurons in GPT2 language models. *Transactions on Machine Learning Research*, 2024. ISSN 2835-8856.
- Søren Hauberg, Oren Freifeld, and Michael Black. A geometric take on metric learning. In *Advances in Neural Information Processing Systems 25*, 2012.
- Jing Huang, Zhengxuan Wu, Christopher Potts, Mor Geva, and Atticus Geiger. RAVEL: Evaluating interpretability methods on disentangling language model representations. In Lun-Wei Ku, Andre Martins, and Vivek Srikumar (eds.), *Proceedings of the 62nd Annual Meeting of the Association for Computational Linguistics (Volume 1: Long Papers)*, pp. 8669–8687, Bangkok, Thailand, August 2024. Association for Computational Linguistics. doi: 10.18653/v1/2024.acl-long.470. URL <https://aclanthology.org/2024.acl-long.470/>.
- Jürgen Jost. *Riemannian Geometry and Geometric Analysis*. Universitext. Springer, 2017.
- Dimitrios Kalatzis, David Eklund, Georgios Arvanitidis, and Soren Hauberg. Variational autoencoders with Riemannian brownian motion priors. In Hal Daumé III and Aarti Singh (eds.), *Proceedings of the 37th International Conference on Machine Learning*, volume 119 of *Proceedings of Machine Learning Research*, pp. 5053–5066. PMLR, 13–18 Jul 2020. URL <https://proceedings.mlr.press/v119/kalatzis20a.html>.
- Subhash Kantamneni and Max Tegmark. Language models use trigonometry to do addition. *arXiv preprint arXiv:2502.00873*, 2025.
- Dhruva Karkada, Daniel J. Korchinski, Andres Nava, Matthieu Wyart, and Yasaman Bahri. Symmetry in language statistics shapes the geometry of model representations, 2026.
- John M. Lee. *Introduction to Smooth Manifolds*, volume 218 of *Graduate Texts in Mathematics*. Springer, 2003.
- John M. Lee. *Introduction to Riemannian Manifolds*, volume 176 of *Graduate Texts in Mathematics*. Springer, 2 edition, 2018.

- Kenneth Li, Oam Patel, Fernanda Viégas, Hanspeter Pfister, and Martin Wattenberg. Inference-time intervention: Eliciting truthful answers from a language model. *Advances in Neural Information Processing Systems*, 36:41451–41530, 2023.
- Samuel Marks and Max Tegmark. The geometry of truth: Emergent linear structure in large language model representations of true/false datasets. In *First Conference on Language Modeling*, 2024. URL <https://openreview.net/forum?id=aa jyHY jjsk>.
- Leland McInnes, John Healy, and James Melville. Umap: Uniform manifold approximation and projection for dimension reduction. *arXiv preprint arXiv:1802.03426*, 2018.
- Alexander Modell, Patrick Rubin-Delanchy, and Nick Whiteley. The origins of representation manifolds in large language models, 2025.
- Kevin R Moon, David Van Dijk, Zheng Wang, Scott Gigante, Daniel B Burkhardt, William S Chen, Kristina Yim, Antonia van den Elzen, Matthew J Hirn, Ronald R Coifman, et al. Visualizing structure and transitions in high-dimensional biological data. *Nature biotechnology*, 37(12): 1482–1492, 2019.
- Core Francisco Park, Andrew Lee, Ekdeep Singh Lubana, Yongyi Yang, Maya Okawa, Kento Nishi, Martin Wattenberg, and Hidenori Tanaka. Iclr: In-context learning of representations. In *International Conference on Learning Representations*, 2025.
- Kiho Park, Yo Joong Choe, and Victor Veitch. The linear representation hypothesis and the geometry of large language models. *arXiv preprint arXiv:2311.03658*, 2023.
- Lucas Prieto, Edward Stevinson, Melih Barsbey, Tolga Birdal, and Pedro A. M. Mediano. From data statistics to feature geometry: How correlations shape superposition, 2026. URL <https://arxiv.org/abs/2603.09972>.
- Shivam Raval, Hae Jin Song, Linlin Wu, Abir Harrasse, Jeff M. Phillips, Fazl Barez, and Amirali Abdullah. Curveball steering: The right direction to steer isn’t always linear, 2026. URL <https://arxiv.org/abs/2603.09313>.
- Nina Rimsky, Nick Gabrieli, Julian Schulz, Meg Tong, Evan Hubinger, and Alexander Turner. Steering llama 2 via contrastive activation addition. In *Proceedings of the 62nd Annual Meeting of the Association for Computational Linguistics (Volume 1: Long Papers)*, pp. 15504–15522, 2024.
- Hang Shao, Abhishek Kumar, and P Thomas Fletcher. The riemannian geometry of deep generative models. In *Proceedings of the IEEE Conference on Computer Vision and Pattern Recognition Workshops*, pp. 315–323, 2018.
- Nishant Subramani, Nivedita Suresh, and Matthew E Peters. Extracting latent steering vectors from pretrained language models. In *Findings of the Association for Computational Linguistics: ACL 2022*, pp. 566–581, 2022.
- Xingzhi Sun, Danqi Liao, Kincaid MacDonald, Yanlei Zhang, Chen Liu, Guillaume Huguet, Guy Wolf, Ian Adelstein, Tim G. J. Rudner, and Smita Krishnaswamy. Geometry-aware generative autoencoders for warped riemannian metric learning and generative modeling on data manifolds, 2025. URL <https://arxiv.org/abs/2410.12779>.
- Joshua B. Tenenbaum, Vin de Silva, and John C. Langford. A global geometric framework for nonlinear dimensionality reduction. *Science*, 290(5500):2319–2323, 2000.
- Alexander Matt Turner, Lisa Thiergart, Gavin Leech, David Udell, Juan J. Vazquez, Ulisse Mini, and Monte MacDiarmid. Steering language models with activation engineering, 2024. URL <https://arxiv.org/abs/2308.10248>.
- Laurens Van der Maaten and Geoffrey Hinton. Visualizing data using t-sne. *Journal of machine learning research*, 9(11), 2008.
- Hieu M. Vu and Tan M. Nguyen. Angular steering: Behavior control via rotation in activation space. *Advances in Neural Information Processing Systems*, 38, 2025.

Zhengxuan Wu, Atticus Geiger, Aryaman Arora, Jing Huang, Zheng Wang, Noah Goodman, Christopher Manning, and Christopher Potts. pyvene: A library for understanding and improving PyTorch models via interventions. In Kai-Wei Chang, Annie Lee, and Nazneen Rajani (eds.), *Proceedings of the 2024 Conference of the North American Chapter of the Association for Computational Linguistics: Human Language Technologies (Volume 3: System Demonstrations)*, pp. 158–165, Mexico City, Mexico, June 2024. Association for Computational Linguistics. doi: 10.18653/v1/2024.naacl-demo.16. URL <https://aclanthology.org/2024.naacl-demo.16/>.

Daniel Wurgaft, Can Rager, Matthew Kowal, Vasudev Shyam, Sheridan Feucht, Usha Bhalla, Tal Haklay, Eric Bigelow, Raphael Sarfati, Thomas McGrath, et al. Manifold steering reveals the shared geometry of neural network representation and behavior. *arXiv preprint arXiv:2605.05115*, 2026.

A METRIC AND SOLVER TAXONOMY TABLES

For reference, we collect here the two taxonomy tables from the framework sections of the main text: table 6 enumerates the three metric instantiations (section 4), and table 7 the (metric, solver) cells we evaluate (section 5).

| | Linear | Labelled spline / G_E on its image | Learned encoder pullback (GAGA) |
|---------------------------|--------|--------------------------------------|--|
| Metric $g(h)$ | I | $J_s^\top J_s$ on $s(\mathbb{R}^k)$ | $J_\phi^\top J_\phi + \epsilon I$ |
| Pulled back from | — | — | learned latent \mathbb{R}^k |
| Ambient dim | 4096 | PCA(64) lifted via P^+ to 4096 | GAGA-PHATE: PCA(64); GAGA-Out: raw-4096 |
| Latent dim k | — | 1 (spline arc) | GAGA-PHATE: 2; GAGA-Out: K (per-task class count) |
| Distance source | — | — | GAGA-PHATE: PHATE on activations; GAGA-Out: Hellinger on outputs |
| Topology prior | none | required | none |
| Per-prompt class labels | no | yes | no (concept-token <i>schema</i> , not per-prompt labels) |
| Per-point cost | $O(1)$ | $O(1)$ | encoder fwd+bwd |
| Generalises off centroids | yes | no | yes |

Table 6: Three metric instantiations reported in this paper. *Linear* is the flat Euclidean baseline. *Labelled spline* is the first fundamental form of a hand-specified cubic-spline parameterisation through labelled centroids (Wurgaft et al., 2026). *Learned encoder pullback (GAGA)* is the surrogate for G_F proposed in this paper; it admits two supervision modes (see section 6.1): **GAGA-PHATE** (PHATE diffusion-potential distance on activations, PCA(64) ambient, latent $k=2$) and **GAGA-Out** (Hellinger distance on outputs over a concept-token schema, raw-4096 ambient, latent $k=K$); GAGA-Out is the empirically winning instantiation. The principled target the GAGA column surrogates, the analytical pullback $G_F = J_F^\top g_y J_F + \epsilon I$ from the behaviour simplex (Wurgaft et al., 2026, Def. 1 eq. 7, under their Hellinger choice $g_y = I$), is discussed in section 4.3 and computed directly on weekdays as a surrogate-validity check (section 8.1). Wurgaft et al. (2026) formalize their manifold steering as the density-based metric G_E (their Def. 1 eq. 6); restricted to the spline’s image, G_E -geodesics agree with the first fundamental form $J_s^\top J_s$ of the spline parameterisation, which is the form we report here.

| | Linear | Labelled spline | GAGA-PHATE | GAGA-Out | Analytical G_F |
|--------------------|--------|-----------------|------------|----------|------------------|
| Closed-form | ✓ | ✓ | — | — | — |
| L-BFGS | — | — | ✓ | ✓ | ✓ |
| Bridge | — | — | ✓ | ◦ | — |

Table 7: The (metric, solver) pairs evaluated in this paper. ✓ = evaluated and reported here; ◦ = planned for the next version; — = not applicable. Linear and labelled-spline have closed-form geodesics; the GAGA metrics admit both the L-BFGS solver and the amortized bridge. GAGA-Out under L-BFGS is the headline method (section 8).

B ACTIVATION EXTRACTION AND DATASET CONSTRUCTION

We extract residual-stream activations from Llama-3.1-8B (Grattafiori et al., 2024) at layer 28 and the last-prompt-token position, using the `causalab baseline` pipeline (Wurgaft et al., 2026) to standardize prompts and counterfactuals across tasks. For each of the four tasks (weekdays, months, letters, ages) the prompt template is the arithmetic form *What is k {units} after z ?*, with k drawn uniformly from the task-specific support and z drawn from the conceptual domain \mathcal{Z} . Per-task prompt counts (after a 5-paraphrase augmentation that increases corpus size without changing the (entity, number) semantic content) are: weekdays 245, months 420, letters \sim 450, ages \sim 4,400

capped at 1,000 for tractability. Train/test split is 80/20 deterministic on seed 42; carrier-prompt sampling at evaluation time is re-seeded per pair on seed 42 so within-pair carrier sets are reproducible.

C PHATE DIFFUSION-DISTANCE CONFIGURATION

We supervise GAGA’s distance-matching loss with PHATE diffusion-potential distances (Moon et al., 2019) computed on the raw 4096-dimensional residual-stream activations. PHATE proceeds in three stages: (a) build a k -nearest-neighbor graph over the activations using Euclidean distance; (b) compute the random-walk transition matrix and raise it to a diffusion time t ; (c) define the *diffusion potential* $\phi_i = -\log P_{i,\cdot}^t$, and take pairwise Euclidean distances between potentials. We use the reference implementation (phate package), with $k = 15$, t chosen by the von Neumann entropy heuristic, no landmark approximation (since per-task corpora are small enough to admit dense computation), and L2 normalization of activations prior to graph construction.² The output is a dense $N \times N$ distance matrix $D = (d_{ij})$ that fixes the target geometry on which we will train the encoder.

D GAGA ARCHITECTURE AND TRAINING

This appendix gives a self-contained description of how we adapt the Geometry-Aware Generative Autoencoder of Sun et al. (2025) to LM activations, with all design choices and hyperparameters specified.

Architecture. The encoder ϕ and decoder ψ are MLPs:

$$\begin{aligned}\phi : \mathbb{R}^{4096} &\rightarrow \mathbb{R}^{1024} \rightarrow \mathbb{R}^{512} \rightarrow \mathbb{R}^{256} \rightarrow \mathbb{R}^{128} \rightarrow \mathbb{R}^k \\ \psi : \mathbb{R}^k &\rightarrow \mathbb{R}^{128} \rightarrow \mathbb{R}^{256} \rightarrow \mathbb{R}^{512} \rightarrow \mathbb{R}^{1024} \rightarrow \mathbb{R}^{4096}\end{aligned}$$

Each hidden layer is followed by BatchNorm and a ReLU; the latent and output projections are linear. The latent dimension k is task-dependent: $k = 2$ for the four 1-D tasks (weekdays, months, letters, ages), and $k = 3$ for the ICLR grid/cylinder tasks of Park et al. (2025). We chose to embed in $k = d_{\text{intrinsic}} + 1$ rather than $k = d_{\text{intrinsic}}$ so that periodic structures (cyclic concepts) can be embedded faithfully without antipodal collapse. The original GAGA targets gene-expression data in $\mathbb{R}^{20 \sim 50k}$ with hidden widths [64, 64, 64]; our wider hidden layers reflect both the larger ambient dimension and the steeper Lipschitz behavior of LM residual streams.

Distance-matching loss. The core supervision matches latent Euclidean distances to PHATE manifold distances:

$$\mathcal{L}_{\text{dist}} = \mathbb{E}_{i \neq j} \left[\left(\|\phi(h_i) - \phi(h_j)\|_2 - d_{ij} \right)^2 \cdot e^{-\alpha d_{ij}} \right], \quad (7)$$

where $\alpha = 0.1$ controls a soft local-distance prior: the exponential weighting attenuates contributions from large d_{ij} , focusing the encoder’s isometry constraint on local geometry, where the manifold tangent plane is a good approximation. With $\alpha = 0$ the loss recovers a global isometry target; with $\alpha \rightarrow \infty$ only k -NN distances are preserved.

Reconstruction and cycle losses. The decoder is tied to the encoder with two further losses:

$$\mathcal{L}_{\text{recon}} = \mathbb{E}_i \left[\|\psi(\phi(h_i)) - h_i\|_2^2 \right], \quad (8)$$

$$\mathcal{L}_{\text{cycle}} = \mathbb{E}_i \left[\|\phi(\psi(\phi(h_i))) - \phi(h_i)\|_2^2 \right]. \quad (9)$$

$\mathcal{L}_{\text{recon}}$ is essential for our intervention pipeline: we steer by sampling waypoints in the latent space, decoding each through ψ , and patching the result into the residual stream. A bad decoder yields “junk” patches even if the latent geometry is correct. $\mathcal{L}_{\text{cycle}}$ is a stabilizer that ensures $\phi \circ \psi \approx \text{id}$ on the latent manifold, preventing the decoder from wandering off the encoder’s image (which would silently break the pullback-metric interpretation).

²L2 normalization is recommended by Moon et al. (2019) for high-dimensional embeddings whose magnitude is informationally redundant; LM residual streams qualitatively satisfy this.

Total loss and weights. The full objective is

$$\mathcal{L} = \lambda_d \mathcal{L}_{\text{dist}} + \lambda_r \mathcal{L}_{\text{recon}} + \lambda_c \mathcal{L}_{\text{cycle}} \quad (10)$$

with $(\lambda_d, \lambda_r, \lambda_c) = (0.9, 0.1, 0.05)$. These weights follow the original GAGA Stage-A recipe (Sun et al., 2025); we add the cycle term (absent in some early GAGA variants) because we observed that the decoder otherwise produces small-norm reconstructions that the LM treats as near-zero patches, suppressing rather than steering behavior.

Training procedure. We sample mini-batches of $B = 256$ activations and form the dense $B \times B$ pairwise distance sub-matrix from the precomputed D on each step (the *point-cloud* dataloader of Sun et al. (2025)). The model is trained with AdamW at learning rate 10^{-3} , weight decay 10^{-4} , and a linear-warmup-then-cosine schedule over up to 300 epochs. Early stopping is triggered on a held-out 20% validation split using $\mathcal{L}_{\text{dist}}$ alone, with a patience of 30 epochs. Final distance-matching accuracy is reported as $1 - \mathbb{E}_{i \neq j} [(\|\phi(h_i) - \phi(h_j)\|_2 - d_{ij})^2] / \text{Var}(d_{ij})$ on the validation split. The per-encoder `pb_demap_r` column of tables 8 and 9 reports this distance-matching quality for the PCA(64) variants on weekdays and months.

GAGA-PHATE vs. GAGA-Hellinger: two encoders, two distance sources. We train two distinct GAGA encoders whose architectures and training procedures are identical except for the distance source $\{d_{ij}\}$ supervising eq. (7):

- **GAGA-PHATE.** d_{ij} = PHATE diffusion-potential distance on the raw 64-D PCA activations (Moon et al., 2019). The encoder pullback $J_\phi^\top J_\phi$ thus reflects activation-space density.
- **GAGA-Hellinger.** d_{ij} = Hellinger distance on per-prompt output distributions, $d_{ij} = \frac{1}{\sqrt{2}} \|\sqrt{p_i} - \sqrt{p_j}\|_2$. The encoder pullback is then trained to track behavioral similarity, and so approximates the behavior-side pullback metric $G_F = J_F^\top J_F + \epsilon I$ of Wurgaft et al. (2026, Def. 1 eq. 7) much more closely than GAGA-PHATE does.

GAGA-Hellinger still differs from the analytical G_F : it pulls back from a 2-D latent rather than from the full simplex $\Delta^{|\mathcal{Z}|}$, and its rank is capped at 2 regardless of $|\mathcal{Z}|$. We treat GAGA-PHATE and GAGA-Hellinger as two cells in the methods grid of table 6.

Differences from Sun et al. (2025). Three substantive deviations from the original GAGA: (1) wider hidden layers to accommodate the larger ambient dimension; (2) the cycle-consistency term described above; (3) PHATE / Hellinger distances are computed once and cached, rather than recomputed per epoch as in some GAGA variants for streaming data settings. We do not use GAGA’s Stage-B (warped metric with discriminator) or Stage-C (Langevin sampling), since our target is interpolation and intervention rather than generation.

E GEODESIC BRIDGE: AMORTIZED GEODESIC COMPUTATION

Given two activation endpoints $h_0, h_1 \in \mathcal{A}$, the geodesic under our learned pullback metric is the minimizer of

$$\arg \min_{\pi} \int_0^1 \|J_\phi(\pi(t)) \dot{\pi}(t)\|_2 dt, \quad \pi(0) = h_0, \pi(1) = h_1. \quad (11)$$

Rather than optimize this per pair, we use the parametric curve module `GeodesicBridge` of Sun et al. (2025), which learns an amortized curve generator c_θ :

$$c_\theta(h_0, h_1, t) = (1-t)h_0 + th_1 + \sigma_q(t) \text{MLP}_\theta(\phi(h_0), \phi(h_1), t), \quad (12)$$

where $\sigma_q(t) = 1 - (2t-1)^q$ is an envelope that vanishes at the endpoints (we use $q = 4$). MLP_θ is a 4-layer MLP of width 256 with ReLU activations. The objective during training is the integrated length eq. (11) on a population of randomly sampled endpoint pairs from the training activations, optionally augmented by a density-weighted term that penalizes excursions through low-density regions:

$$\mathcal{L}_{\text{bridge}}(\theta) = \mathbb{E}_{(h_0, h_1)} \left[\int_0^1 \|J_\phi(c_\theta(t)) \dot{c}_\theta(t)\|_2 dt + \mu \int_0^1 \rho(c_\theta(t))^{-1} dt \right], \quad (13)$$

with ρ a kernel-density estimate on the training activations and $\mu = 0.05$. The first term is the length under the pullback metric; the second is the density-weighted term that keeps geodesics on-manifold even when the encoder Jacobian is locally near-singular. We train for 50,000 steps with Adam at learning rate 10^{-3} , batches of 64 endpoint pairs, and a discretization of $T = 32$ time steps per curve.

F AUTODIFF GEODESICS: SOLVER AND ANALYTICAL J_F IMPLEMENTATION

This appendix gives concrete implementation details for the two solver/metric ingredients introduced in sections 4.3 and 5: the L-BFGS free-waypoint solver, and the analytical J_F metric used in its highest-fidelity instantiation.

F.1 FREE-WAYPOINT PATH PARAMETERIZATION

Given two fixed endpoints $h_0, h_1 \in \mathcal{A}$ and a number of discretization steps K , the path is represented as

$$\pi = (\pi_0, \pi_1, \dots, \pi_K), \quad \pi_0 = h_0, \pi_K = h_1,$$

with the $K - 1$ interior waypoints $\{\pi_1, \dots, \pi_{K-1}\}$ as the only optimized parameters. Initialization is the linear interpolation $\pi_k^{(0)} = (1 - k/K) h_0 + (k/K) h_1$, so the optimization starts at the straight-line baseline. We use $K = 50$ throughout to match the steering resolution of Wurgaft et al. (2026). This is the parameterization the L-BFGS solver uses in practice; a Bernstein-basis Bézier variant with $C = 8$ control points yields qualitatively identical geodesics in preflight checks but has a marginally rougher length landscape and is not reported.

F.2 DISCRETE LENGTH FUNCTIONAL AND L-BFGS

Given a metric $g(h) = J(h)^\top J(h)$ at each waypoint, the discrete length to minimize is

$$L(\pi) = \sum_{k=0}^{K-1} \sqrt{\|J(\pi_k) \Delta_k\|_2^2 + \epsilon \|\Delta_k\|_2^2}, \quad \Delta_k = \pi_{k+1} - \pi_k, \quad (14)$$

with ϵ a small regularizer absorbing rank deficiency. The right-hand factored form keeps memory at $O(K \cdot m \cdot D)$ with $m = \text{rank}(J) \leq |\mathcal{Z}| + 1 \ll D$, instead of the $O(K \cdot D^2)$ that an explicit $G = J^\top J$ matrix would require.

We use the freeze-metric approximation: at each L-BFGS iteration, $J(\pi_k)$ is recomputed at the current waypoint but *detached from the optimizer’s computation graph* (Arvanitidis et al., 2018). Gradients therefore flow only through the Δ_k in the outer norm, not through the metric’s dependence on π_k . This is the standard discrete-Riemannian choice; it gives a Newton-like step on a frozen quadratic form and avoids the second-order gradient terms that would otherwise be required.

Optimizer settings: `torch.optim.LBFGS` with `lr=1.0`, `max_iter=200`, `tolerance_grad=1e-6`, `tolerance_change=1e-6`, `history_size=20`, and `line_search_fn='strong_wolfe'`. A single `optimizer.step(closure)` call runs the full 200 internal iterations; interior waypoints are the only parameters, with endpoints re-attached via `torch.cat` at each closure evaluation. Gradient clipping at $\|g\|_\infty \leq 1.0$ prevents the path-collapse failure mode mentioned in section 5.

F.3 ANALYTICAL J_F METRIC

The metric specified in Wurgaft et al. (2026, Def. 1 eq. 7) is

$$G_F(h) = J_F(h)^\top g_y J_F(h) + \epsilon I,$$

where $F : \mathcal{A} \rightarrow \mathcal{Y}$ is the rest-of-the-network forward map (layer-28 activations to output distribution restricted to the concept domain plus an “other” bin). We compute this metric exactly, with the following choices.

Hellinger output coordinates make $g_y = I$. We define $F(h) = \sqrt{\text{softmax}(\text{logits}[\mathcal{Z} \cup \{\text{other}\}])}$: the LM forward pass restricted to concept tokens, with $\sqrt{\cdot}$ applied so that outputs live in Hellinger coordinates. Under this parameterization the natural behavior-space metric is the identity: $g_y = I$, since Hellinger distance is Euclidean distance on \sqrt{p} . G_F then reduces to $J_F^\top J_F + \epsilon I$.

Row-by-row Jacobian extraction. $J_F \in \mathbb{R}^{(|\mathcal{Z}|+1) \times D}$ is computed row-by-row via `torch.autograd.grad` with `retain_graph=True`: one backward pass per concept-token output (plus one for the “other” bin), each producing one row of J_F . We use this in preference to `torch.func.jacrev` or `torch.func.jacfwd` because their functionalization requirements interact awkwardly with the subspace-replacement injection (section F.4) of pre-computed PCA activations into a wrapped forward pass.

Carrier handling. G_F is carrier-dependent: the rest-of-network tail attends to the carrier prompt’s context, so $J_F(h)$ is defined relative to a prompt. For the L-BFGS optimization we pin a *single canonical carrier* — the first test-split prompt, shared across all centroid pairs; an expectation of J_F over carriers is the costlier principled variant and is left to future work. Evaluation of E_{BC} at the resulting waypoints still averages over all 16 carriers as for the other methods, so per-pair E_{BC} values remain directly comparable across methods.

ϵ regularizer. We default to $\epsilon = 10^{-3}$. The rank cap $\text{rank}(J_F) \leq |\mathcal{Z}| + 1$ ensures that the unregularized $J_F^\top J_F$ is singular on the $D - |\mathcal{Z}| - 1$ dimensional nullspace; ϵI on this nullspace defines a small but nonzero length on directions invisible to F , which prevents the path from escaping into that nullspace under optimization. Sensitivity to ϵ is reported on a long-hop pair in section H.

Compute. ~ 3 GPU-minutes per pair on a single A100 for weekdays ($|\mathcal{Z}| = 7$); larger concept schemas cost proportionally more. For comparison, GAGA encoder Jacobian extraction is ~ 30 seconds per pair, and the GeodesicBridge inference is ~ 50 milliseconds per pair — the learned surrogate is by far the cheaper metric to evaluate. We report the analytical- G_F cell on weekdays (all 21 centroid pairs).

F.4 SUBSPACE-REPLACEMENT INJECTION

All optimization happens in the PCA(64) subspace, but the LM expects \mathbb{R}^{4096} activations. For a waypoint $\pi_k \in \mathbb{R}^{64}$ and a carrier prompt’s unintervened layer-28 last-token activation $h_{\text{orig}} \in \mathbb{R}^{4096}$, the injected activation is

$$h_{\text{inj}} = h_{\text{orig}} + (\pi_k - P h_{\text{orig}}) P^{-1},$$

implementing *replacement* of the in-PCA-subspace component while *preserving* the off-subspace component. In code, `h_orig + (pi_k - h_orig @ pca.components_.T) @ pca.components_`. This matches causalab’s `FeatureInterpolateIntervention` semantics and is the same lift used by all methods (linear, spline, GAGA, autodiff), so per-pair E_{BC} differences are purely method-attributable.

F.5 COMPARISON PROTOCOL

For each task and method, we compute paths over the same set of centroid pairs (all $\binom{N}{2}$ for weekdays and months; 50 sampled pairs for letters and ages, seed 42) and report:

- Mean residual between paths after projecting both into the first three principal components of the activation distribution.
- Per-pair E_{BC} averaged across 16 carrier prompts, with paired t -tests across methods on the per-pair E_{BC} arrays.
- Within-metric solver consistency: GAGA-PHATE + L-BFGS vs. GAGA-PHATE + Bridge under the same metric, expected to agree within $2\times$ on E_{BC} if both solvers converge.

The full metric-by-solver comparison table appears in table 7.

F.6 SPLINE AS A DEGENERATE SPECIAL CASE

The spline geodesic of Wurgaft et al. (2026) can be recovered from eq. (14) by (a) restricting π to the parametric spline family with control points at the labeled centroids; (b) replacing g with the metric implicitly induced by the spline’s path-length functional; (c) replacing the optimization with closed-form interpolation through the (label-ordered) centroids. Removing each of these restrictions in turn defines an intermediate baseline. We report only the fully unrestricted autodiff variant in the main body; an ablation grid over the three restrictions is in section H.

G ENCODER-VARIANT ABLATION: PCA(64) GAGA ENCODERS ARE INERT

This appendix reports the full per-encoder matrix referenced from section 8.5 (15 PCA(64) encoder variants \times 4 tasks, 1 rep, 5 shards/cell), tabulated in tables 8 and 9. Coverage at the time of writing: weekdays 15/15, months 7/15 (GAGA-PHATE + Vanilla; GAGA-Hellinger and $\lambda=10$ not yet run); letters 0/15, ages 0/15 deferred (the GAGA-Out rows for letters/ages already lose E_{BC} to the baselines, so the PCA(64) sweep there is lower priority). **GAGA-Out** rows are the frozen headline numbers (tables 2 and 3) reused as a reference, not re-run for this ablation. All numbers are mean across $n = 21$ pairs (weekdays) or $n = 50$ (months); paired- t compares each encoder’s GAGA path against the linear baseline (more negative $t =$ more natural).

Table 8: Weekdays: 15/15 PCA(64) encoder variants vs. the raw-4096 GAGA-Out reference. “pb_demap_r” is the Pearson correlation between encoder-pullback distances and the supervision distance (training diagnostic). E_{BC} , legibility, target-prob and top-1@end are all indistinguishable from the linear baseline ($E_{BC} = 0.0995$, legibility = 0.040, tgt_prob_end = 0.049, top-1@end = 0.286) for every PCA(64) variant.

| encoder | pb_demap_r | E_{BC}^{gaga} | $t(g - \text{lin})$ | legib top-1 | tgt_prob_end | top-1@end |
|---------------------------------|------------|-----------------|---------------------|--------------|---------------|--------------|
| GAGA-Out (raw-4096, ref) | 0.929 | 0.00846 | -34.1 | 1.000 | 0.2023 | 0.762 |
| Vanilla-AE | 0.317 | 0.09951 | -0.35 | 0.049 | 0.0488 | 0.286 |
| GAGA-PHATE $\lambda=0.1$ | 0.687 | 0.09954 | +0.99 | 0.050 | 0.0488 | 0.286 |
| GAGA-PHATE $\lambda=1$ | 0.444 | 0.09961 | +2.67 | 0.050 | 0.0488 | 0.286 |
| GAGA-PHATE $\lambda=10$ | 0.320 | 0.09961 | +4.10 | 0.050 | 0.0488 | 0.286 |
| GAGA-PHATE $\lambda=50$ | 0.343 | 0.09954 | +1.09 | 0.049 | 0.0488 | 0.286 |
| GAGA-PHATE $\lambda=100$ | 0.349 | 0.09958 | +2.77 | 0.049 | 0.0488 | 0.286 |
| GAGA-PHATE $\lambda=250$ | 0.335 | 0.09958 | +3.20 | 0.049 | 0.0488 | 0.286 |
| GAGA-PHATE $\lambda=500$ | 0.331 | 0.09956 | +1.93 | 0.049 | 0.0488 | 0.286 |
| GAGA-Hellinger $\lambda=0.1$ | 0.377 | 0.09956 | +1.77 | 0.050 | 0.0488 | 0.286 |
| GAGA-Hellinger $\lambda=1$ | 0.471 | 0.09966 | +3.33 | 0.049 | 0.0488 | 0.286 |
| GAGA-Hellinger $\lambda=10$ | 0.462 | 0.09956 | +1.52 | 0.050 | 0.0488 | 0.286 |
| GAGA-Hellinger $\lambda=50$ | 0.462 | 0.09957 | +1.81 | 0.049 | 0.0488 | 0.286 |
| GAGA-Hellinger $\lambda=100$ | 0.456 | 0.09955 | +1.17 | 0.049 | 0.0488 | 0.286 |
| GAGA-Hellinger $\lambda=250$ | 0.463 | 0.09957 | +2.03 | 0.050 | 0.0488 | 0.286 |
| GAGA-Hellinger $\lambda=500$ | 0.464 | 0.09962 | +2.68 | 0.050 | 0.0488 | 0.286 |
| Linear (PCA(64), reference) | — | 0.09952 | — | 0.040 | 0.0488 | 0.286 |
| Labelled spline (PCA(64), ref) | — | 0.09956 | — | 0.047 | 0.0488 | 0.286 |

Reading the matrix. Across two supervision targets (GAGA-PHATE, GAGA-Hellinger), seven λ_{dist} values from 0.1 to 500, and the plain-reconstruction Vanilla-AE, every finished PCA(64) encoder produces E_{BC} within $\sim 10^{-4}$ of the linear baseline, identical legibility (≈ 0.05 weekdays, ≈ 0.13 months), and identical endpoint target probability (0.049 weekdays, 0.128 months). The pb_demap_r column shows that several encoders do learn the supervision distance reasonably well (e.g. GAGA-PHATE $\lambda=0.1$ on weekdays at $r = 0.69$), but learning the distance does not translate into steering, because the lifted PCA(64) endpoint is not an activation the language model would naturally produce for the target class. Only the raw-4096 GAGA-Out encoder (where the geodesic, the lift, and the model all live in the same ambient space) separates from the baselines on every metric. The months GAGA-Hellinger family and the letters/ages PCA(64) sweeps are left to future work; the GAGA-Out rows for letters/ages already lose E_{BC} to the baselines (table 2), so completing the PCA(64) sweep there is unlikely to overturn the headline.

Table 9: Months: 7/15 PCA(64) encoder variants finished (GAGA-PHATE family and Vanilla-AE; GAGA-Hellinger cells and $\lambda=10$ not yet run). Same inert-vs-linear pattern as weekdays.

| encoder | pb_demap_r | E_{BC}^{gaga} | $t(g - \text{lin})$ | legib top-1 | tgt_prob_end | top-1@end |
|---------------------------------|------------|------------------------|---------------------|--------------|---------------|-----------|
| GAGA-Out (raw-4096, ref) | 0.975 | 0.04558 | -24.76 | 1.000 | 0.4665 | 1.000 |
| Vanilla-AE | 0.286 | 0.11158 | -0.71 | 0.125 | 0.1277 | 1.000 |
| GAGA-PHATE $\lambda=0.1$ | 0.426 | 0.11165 | +3.72 | 0.125 | 0.1277 | 1.000 |
| GAGA-PHATE $\lambda=1$ | 0.028 | 0.11167 | +4.70 | 0.127 | 0.1277 | 1.000 |
| GAGA-PHATE $\lambda=10$ | -0.014 | — not run | — | — | — | — |
| GAGA-PHATE $\lambda=50$ | 0.039 | 0.11164 | +2.53 | 0.125 | 0.1277 | 1.000 |
| GAGA-PHATE $\lambda=100$ | 0.023 | 0.11166 | +3.01 | 0.125 | 0.1277 | 1.000 |
| GAGA-PHATE $\lambda=250$ | 0.037 | 0.11165 | +3.02 | 0.127 | 0.1277 | 1.000 |
| GAGA-PHATE $\lambda=500$ | 0.050 | 0.11164 | +2.29 | 0.125 | 0.1277 | 1.000 |
| Linear (PCA(64), reference) | — | 0.11159 | — | 0.125 | 0.1277 | 1.000 |
| Labelled spline (PCA(64), ref) | — | 0.11524 | — | 0.177 | 0.1277 | 1.000 |

H HYPERPARAMETER SENSITIVITY

We report sensitivity of the headline number E_{BC} to: (1) latent dimension $k \in \{2, 3, 4\}$; (2) PHATE $k\text{NN} \in \{5, 10, 15, 30\}$; (3) GAGA decay rate $\alpha \in \{0, 0.05, 0.1, 0.2, 0.5\}$; (4) bridge density weight $\mu \in \{0, 0.01, 0.05, 0.1\}$. A full sensitivity sweep across these four hyperparameters is left to future work; pilot studies on weekdays indicated that the headline ordering is robust within reasonable ranges of each.

I COMPUTATIONAL COMPLEXITY

Table 10 compares the asymptotic cost of computing one geodesic between an endpoint pair, across the (metric, solver) cells of table 7. Let D be the ambient activation dimension ($D = 4096$), K the number of path waypoints ($K = 50$), m the rank of the metric Jacobian ($m \leq |\mathcal{Z}| + 1 \ll D$), and T the number of L-BFGS iterations. Write \mathcal{E} for the cost of one encoder forward-or-backward pass, \mathcal{F} for one forward-or-backward pass through the rest-of-network behaviour map F (only the ~ 3 -layer tail downstream of the injection layer; section 4.3), and \mathcal{B} for one pass through the amortized bridge curve generator. The behaviour-map pass is far more expensive than the encoder pass: $\mathcal{F} \gg \mathcal{E}$.

| Metric + solver | Per-pair geodesic | One-time / amortized |
|-------------------------------|------------------------|---------------------------------|
| Linear (closed form) | $O(KD)$ | — |
| Labelled spline (closed form) | $O(KD)$ | $O(\mathcal{Z} D)$ spline fit |
| GAGA + L-BFGS | $O(T K m \mathcal{E})$ | encoder training |
| GAGA + Bridge | $O(K \mathcal{B})$ | encoder and bridge training |
| Analytical G_F + L-BFGS | $O(T K m \mathcal{F})$ | none (metric is the LM) |

Table 10: Asymptotic cost of computing one geodesic. The closed-form baselines are linear in the path size KD . The L-BFGS solvers run T optimizer steps, each evaluating the metric Jacobian at the K waypoints via m vector–Jacobian products, with working memory $O(KmD)$ (section 5). The bridge amortizes the per-pair optimization into a single forward pass, after a one-time training. Analytical G_F shares the L-BFGS solver’s complexity but evaluates the behaviour-map Jacobian, paying $\mathcal{F} \gg \mathcal{E}$ at every step — \mathcal{F}/\mathcal{E} is roughly 10^3 , a three-block transformer pass (plus the unembedding) against a small MLP: the quantitative reason a learned encoder is used as a cheap surrogate for G_F .

J ADDITIONAL FIGURES

This appendix collects per-task path visualizations referenced from section 8, plus the GAGA-Out training-loss curves (fig. 2). Each figure projects activation-space trajectories onto the top

principal components of the per-task training-prompt activation distribution, so visual comparisons across methods are made in the same coordinate frame. Linear paths appear as straight chords, the labeled cubic spline as a smooth curve through every class centroid, and the GAGA geodesic as the decoded output of the trained `GeodesicBridge` module evaluated at $K = 50$ time steps. Where multiple paraphrases of the same prompt are shown, each paraphrase’s unintervened layer-28 activation contributes its own off-subspace component during the lift back to \mathbb{R}^{4096} (section F.4), so different paraphrases trace slightly different 4096-D trajectories even though they all share the same in-PCA-subspace waypoints.

J.1 GAGA-OUT TRAINING-LOSS CURVES

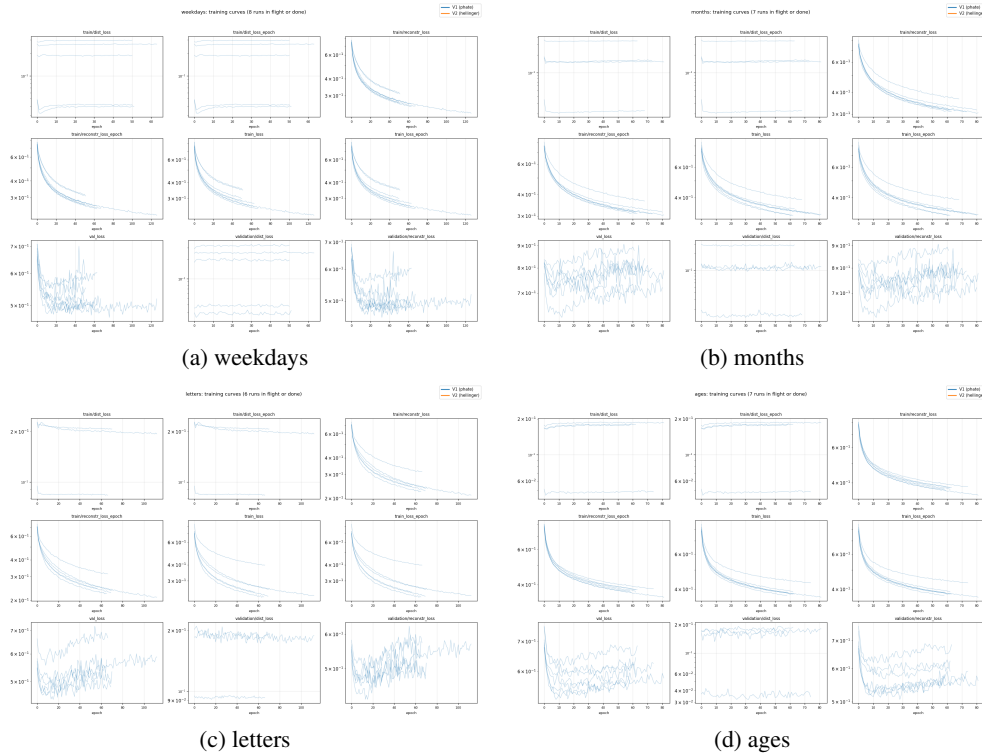


Figure 2: Per-task training curves for the GAGA-Out encoder (seed0), one panel per task. Each panel plots the distance-matching loss $\mathcal{L}_{\text{dist}}$ together with the reconstruction and cycle terms on training and held-out validation splits across epochs, under the linear-warmup-then-cosine schedule of section D. These are the runs whose frozen checkpoints produce every GAGA-Out number in section 8.

J.2 ACTIVATION-SPACE 2-D PATH PROJECTIONS PER TASK

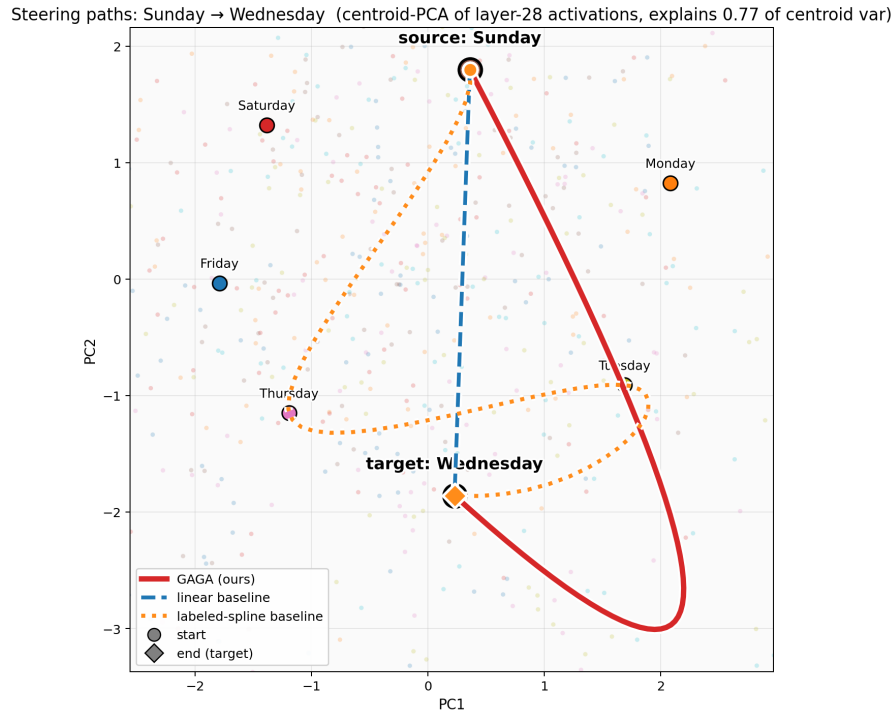


Figure 3: **Weekdays** (cyclic, $|\mathcal{Z}| = 7$): activation-space paths for the example pair Sunday → Wednesday, projected onto the top two principal components of the per-prompt PCA(64) activations. Background grey points are the training-prompt activations; coloured points mark per-class centroids. Three paths are overlaid: the Euclidean chord (linear), the labeled cubic spline through all seven centroids in PCA(64), and the GAGA-PHATE geodesic decoded from the trained bridge. The GAGA path threads the training-prompt cloud, while the linear and labeled-spline paths leave it. This is the visual signature of the on-manifold behaviour of the GAGA geodesic.

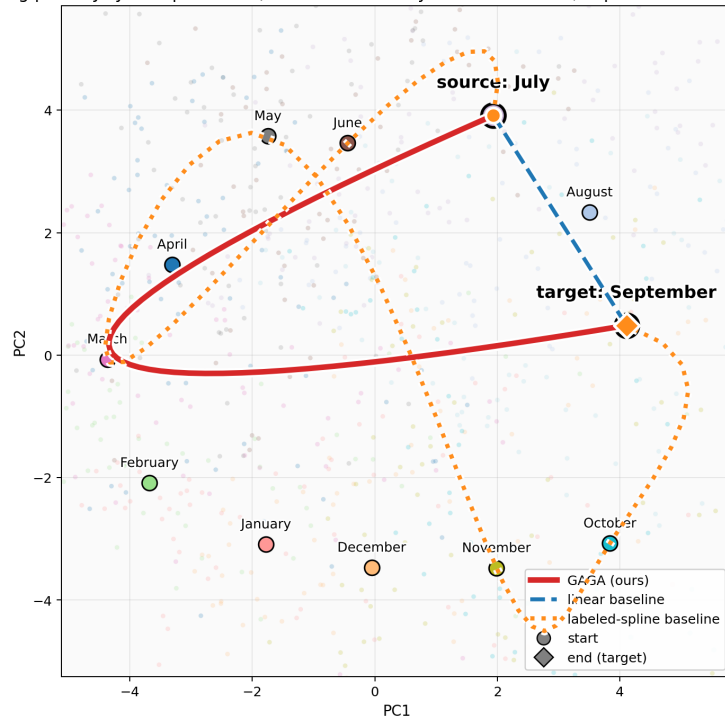
Steering paths: July \rightarrow September (centroid-PCA of layer-28 activations, explains 0.59 of centroid var)

Figure 4: **Months** (cyclic, $|\mathcal{Z}| = 12$): activation-space paths for the example pair July \rightarrow September. Same conventions as fig. 3. The labeled spline curls aggressively along the labeled cycle (visible as the wider arc passing through August’s centroid), while the GAGA geodesic takes a shorter on-manifold route that still produces lower E_{BC} at every waypoint (table 2). The spline’s longer behavior-space arc (table 4) is a consequence of this aggressive curvature, not of better steering: the longer arc passes through low-density activation regions and produces unnaturally smeared output distributions in behavior space.

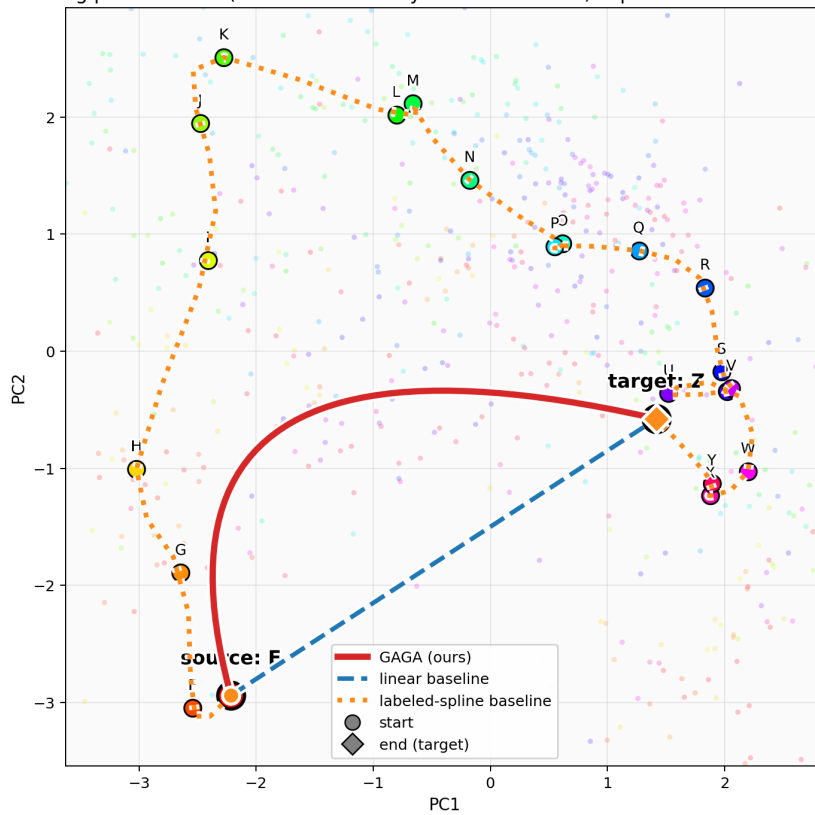
Steering paths: E \rightarrow Z (centroid-PCA of layer-28 activations, explains 0.46 of centroid var)

Figure 5: **Letters** (sequential, $|\mathcal{Z}| = 22$): activation-space paths for the longest sequential pair $E \rightarrow Z$. Same conventions as fig. 3. With 22 well-separated sequential centroids, the labeled spline becomes a much longer curve and drifts further from the training-prompt cloud than on weekdays/months; GAGA’s geodesic stays close throughout.

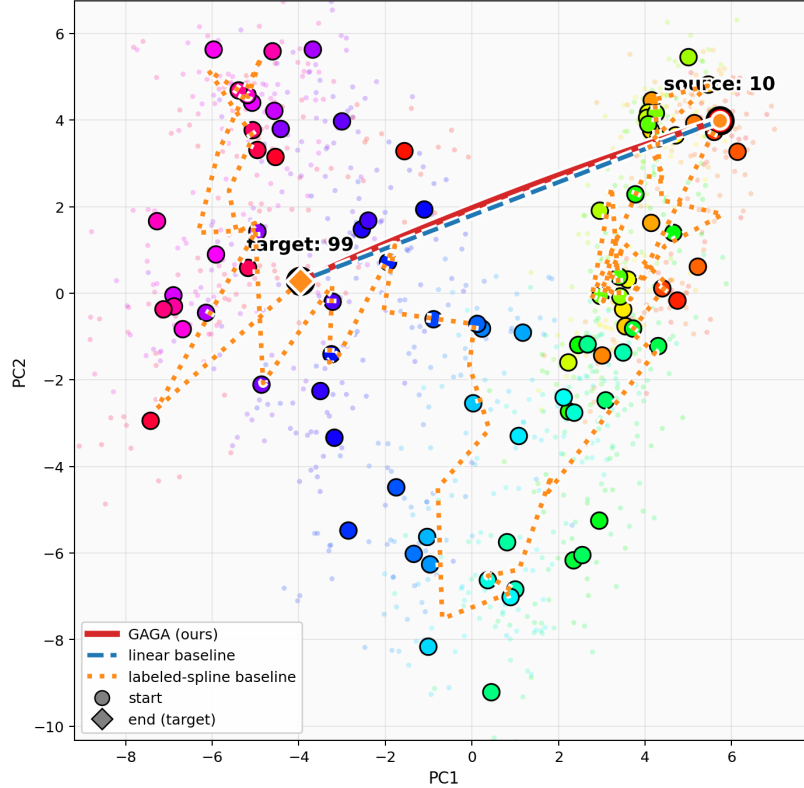
Steering paths: 10 \rightarrow 99 (centroid-PCA of layer-28 activations, explains 0.16 of centroid var)

Figure 6: **Ages** (sequential, $|\mathcal{Z}| \approx 91$): activation-space paths for the long-hop pair age-10 \rightarrow age-99. Same conventions as fig. 3. With ~ 91 sequential centroids, the labeled cubic spline curls dramatically through each centroid in order; in the 2-D projection shown here, the path visibly visits intermediate ages 10, 11, 12, \dots , 99, which is why the labeled spline scores 95% on the visit-intermediates rate (table 4). The cost: the spline’s behaviour-space arc length is 8.13 on this task, exceeding the unit Hellinger-simplex diameter and indicating that the curved path overshoots the natural output distribution. GAGA-Out takes a much shorter route (1.09 in behaviour-space arc), sacrifices the strict semantic-progression property, and is also the task on which GAGA-Out *loses* E_{BC} to both baselines (table 2: 0.53 vs. 0.19 linear).

J.3 PATH CONSISTENCY ACROSS PARAPHRASES

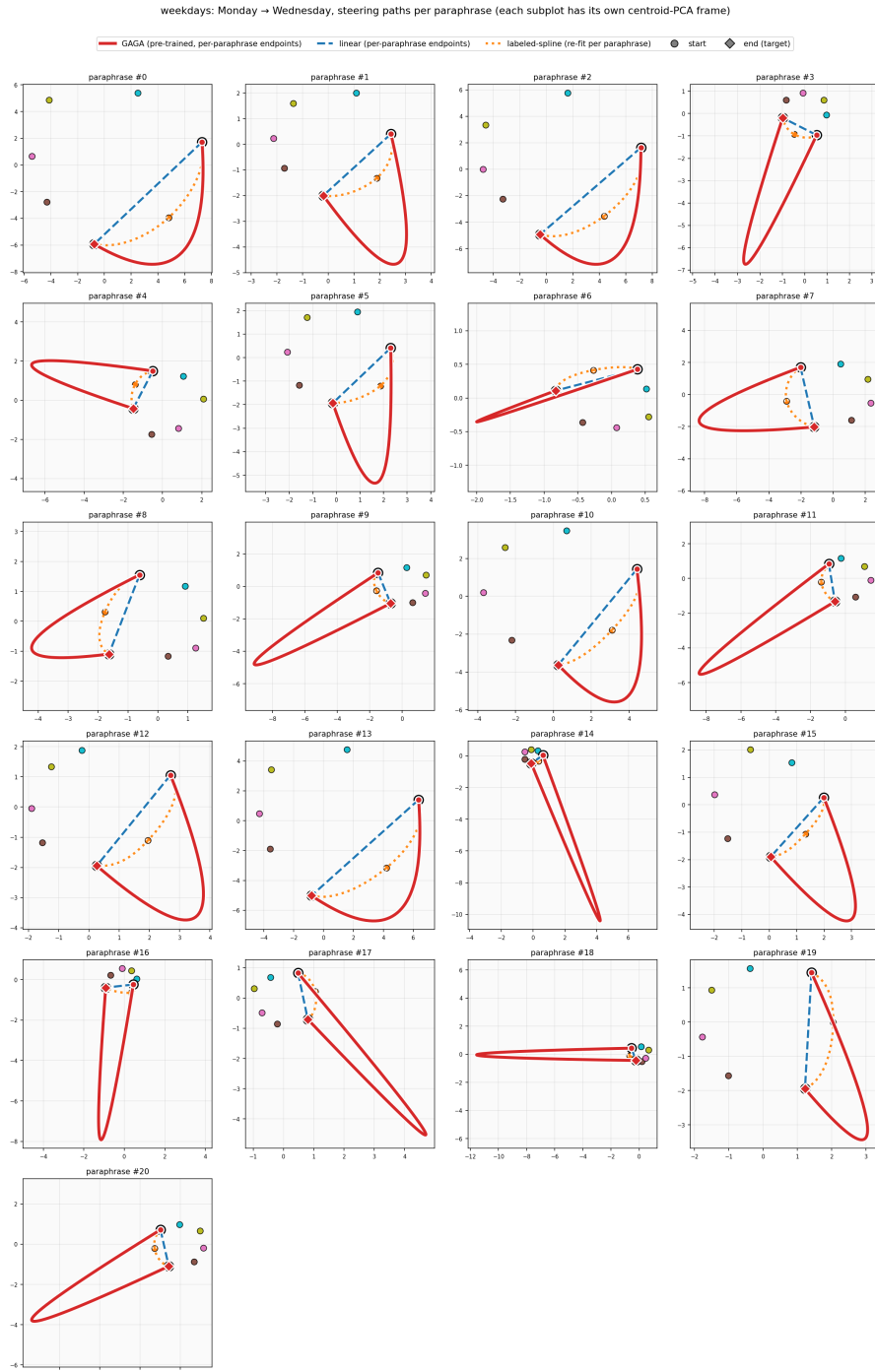


Figure 7: Weekdays, paraphrase consistency (Monday → Wednesday). Each of the prompt paraphrases used during GAGA training contributes its own off-subspace component during the lift back to \mathbb{R}^{4096} (section F.4). We project the resulting 4096-D trajectories onto the same per-task PC frame as fig. 3 and overlay paths for several paraphrases of the same prompt. GAGA’s geodesic varies only slightly across paraphrases (the off-subspace component is small and consistent across paraphrases of the same arithmetic question), while linear and spline paths inherit substantially more variation. This is a sanity check that the manifold structure GAGA learns is paraphrase-invariant in the intended way.

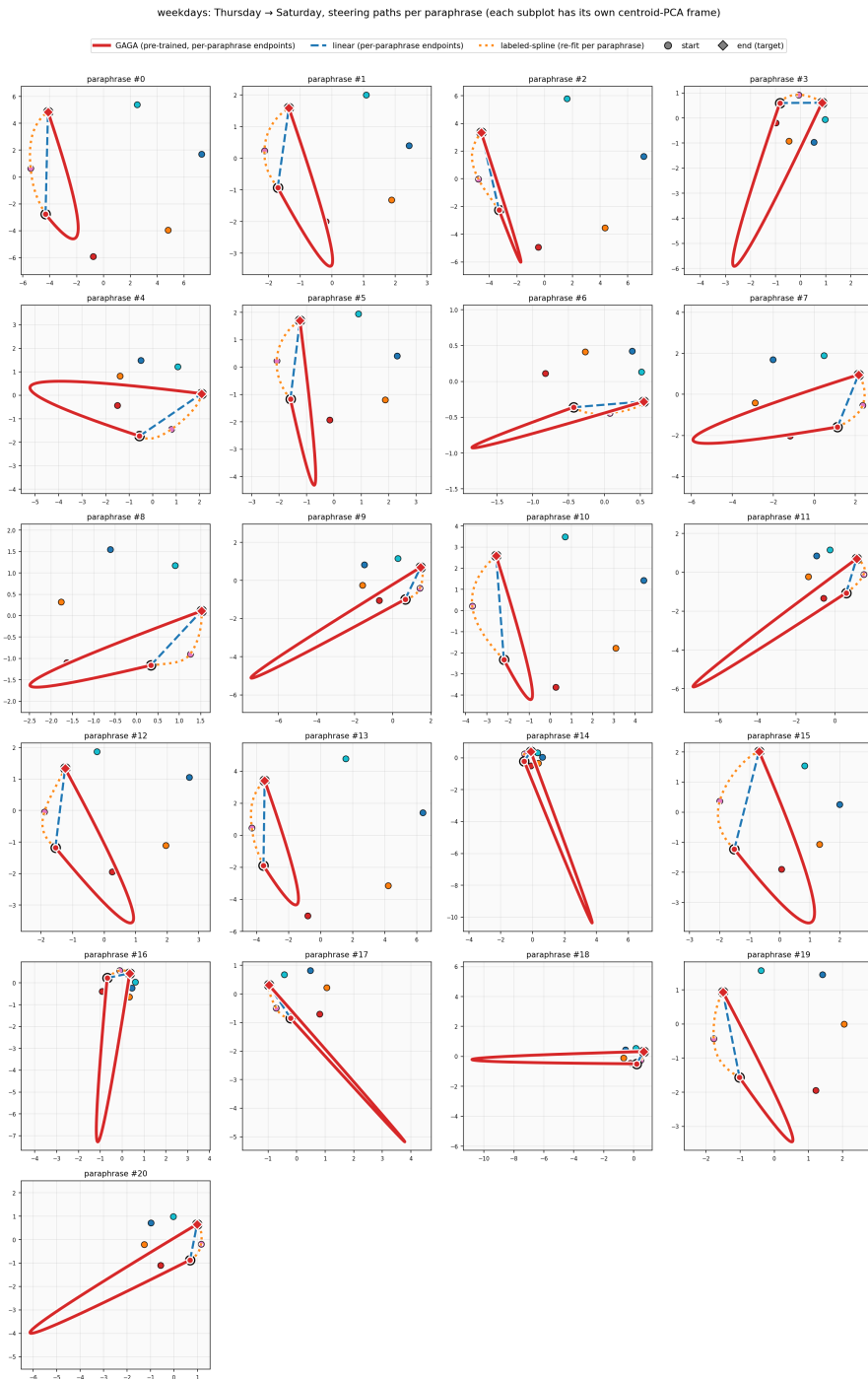


Figure 8: **Weekdays, paraphrase consistency** (Thursday → Saturday). Same conventions as fig. 7. We include a second example pair to confirm the paraphrase-invariance behaviour is not specific to the Monday → Wednesday pair.

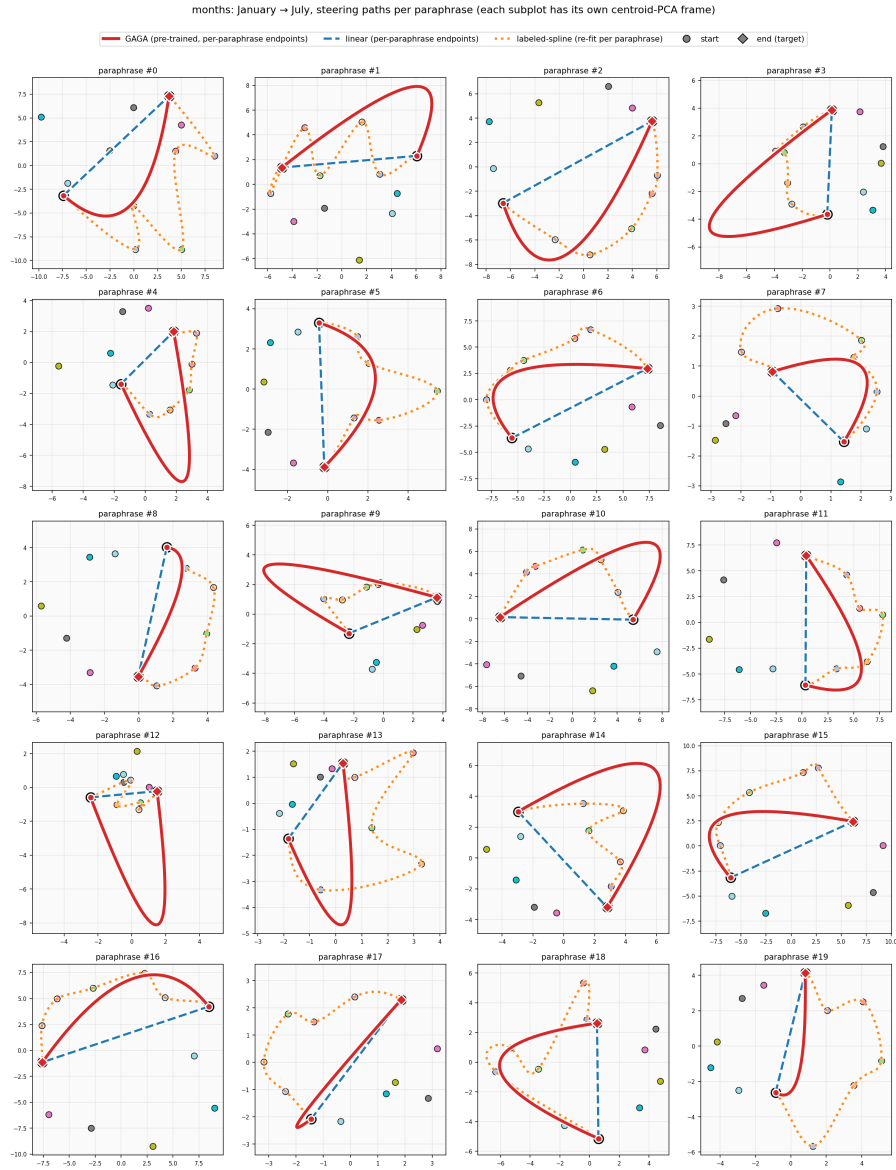


Figure 9: **Months, paraphrase consistency** (January → July). Same conventions as fig. 7, on the months task. The longer cyclic shortest-path (six hops) magnifies inter-method differences: the labeled spline’s paraphrase variation clearly grows along the curve, while GAGA’s stays compact.

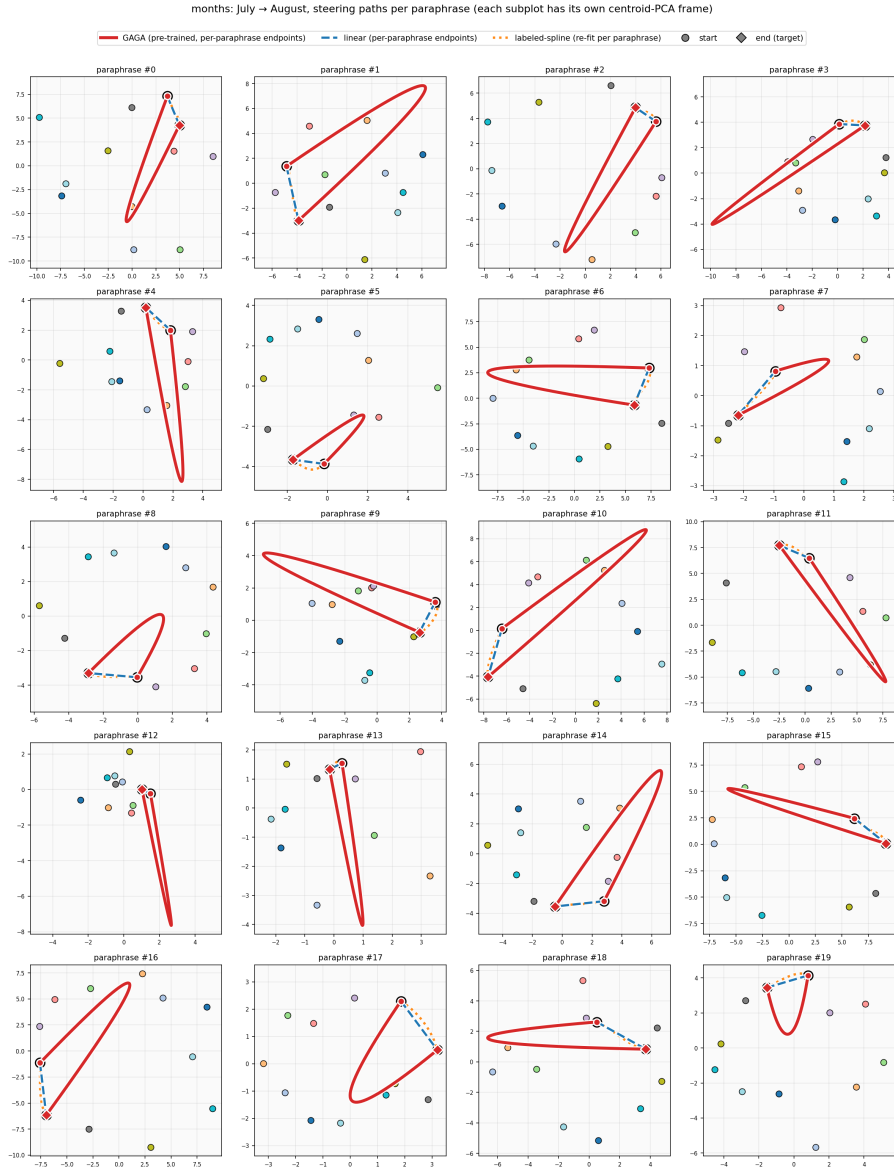


Figure 10: **Months, paraphrase consistency** (July → August). A short-hop counterpart to fig. 9. With only one cyclic hop the three methods are visually closer; even here the GAGA path is the tightest across paraphrases.

J.4 CYCLIC GEOMETRY PER PARAPHRASE

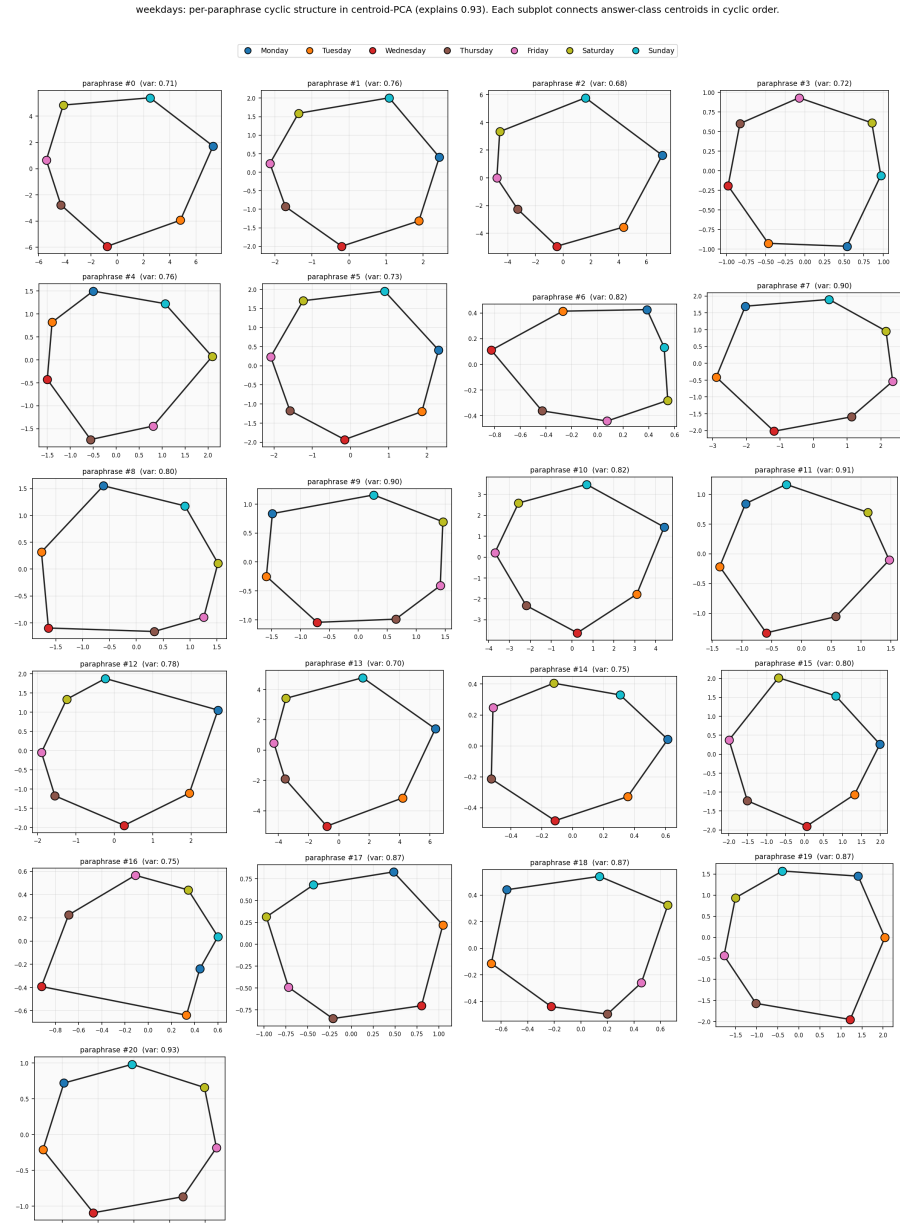


Figure 11: Weekdays, cyclic latent geometry per paraphrase. We plot the GAGA-PHATE latent (\mathbb{R}^2) embedding of training-prompt activations, coloured by ground-truth weekday and panelled by paraphrase template. The seven centroids consistently arrange around a closed loop in latent space across paraphrases, even though paraphrases are not aligned in any explicit cyclic-invariance loss; the cyclic structure is recovered from PHATE diffusion distances alone. This figure complements fig. 3 by showing that the manifold structure GAGA recovers is not an artifact of a particular prompt phrasing.

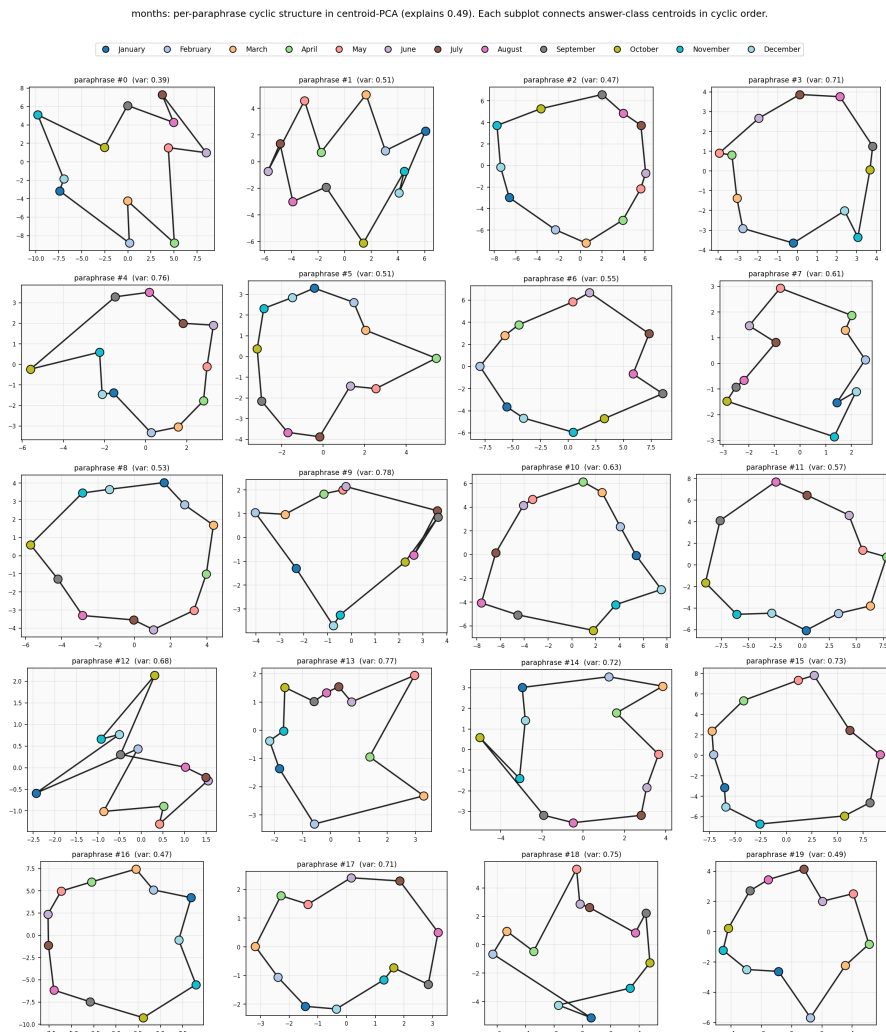


Figure 12: **Months, cyclic latent geometry per paraphrase.** Same conventions as fig. 11. Twelve months arrange around the latent cycle with visible inter-paraphrase consistency. Two qualitative observations: (i) cyclic spacing is not uniform: summer months (June–August) tend to sit closer together than winter months, suggesting the underlying activation density on \mathcal{M}_h is non-uniform; (ii) the cycle is consistently *recovered* but with a small per-paraphrase rotation, reflecting that PHATE’s local geometry is paraphrase-invariant up to a global symmetry.